

Controlled surface reconstruction on ferromagnetic oxides: spin pinning effect to the oxyhydroxide layer and its enhanced oxygen evolution activity

Tianze Wu^{1,2,3,Δ}, Xiao Ren^{1,2,Δ}, Yuanmiao Sun², Shengnan Sun², Guoyu Xian¹, Günther G. Scherer^{4,5}, Adrian C. Fisher⁶, Daniel Mandler^{7,8}, Joel W. Ager^{9,10}, Alexis Grimaud^{11,12}, Junling Wang², Chengmin Shen¹, Haitao Yang^{1*}, Jose Gracia¹³, Hong-Jun Gao¹, Zhichuan J. Xu^{2,3,14*}

¹Beijing National Laboratory for Condensed Matter Physics and Institute of Physics, Chinese Academy of Science, Beijing 100190, China;

²School of Materials Science and Engineering, Nanyang Technological University, 50 Nanyang Avenue, 639798, Singapore;

³Solar Fuels Laboratory and Energy Research Institute, Nanyang Technological University, 50 Nanyang Avenue, 639798, Singapore;

⁴Department for Management of Science and Technology Development, Ton Duc Thang University, Ho Chi Minh City, Vietnam;

⁵Faculty of Applied Sciences, Ton Duc Thang University, Ho Chi Minh City, Vietnam;

⁶Department of Chemical Engineering, University of Cambridge, Cambridge CB2 3RA, UK;

⁷Institute of Chemistry, The Hebrew University of Jerusalem, Jerusalem 9190401, Israel;

⁸Singapore-HUJ Alliance for Research and Enterprise (SHARE), Nanomaterials for Energy and Energy-Water Nexus (NEW), Campus for Research Excellence and Technological Enterprise (CREATE), 138602, Singapore;

⁹Department of Materials Science and Engineering, University of California at Berkeley, Berkeley, California 94720, USA;

¹⁰Berkeley Educational Alliance for Research in Singapore (BEARS), Ltd., 1 CREATE Way, 138602, Singapore

¹¹Chimie du Solide et de l'Energie, UMR 8260, Collège de France, 75231 Paris Cedex 05, France;

¹²Réseau sur le Stockage Electrochimique de l'Energie (RS2E), CNRS FR 3459, 33 rue Saint Leu, 80039, Amiens Cedex, France;

¹³MagnetoCat SL, General Polavieja 9 3I, 03012 Alicante, Spain;

¹⁴Energy Research Institute @ Nanyang Technological University, 50 Nanyang Avenue, Singapore 639798, Singapore.

^ΔThese authors contribute equally to this work.

*Corresponding authors: xuzc@ntu.edu.sg (Z. Xu), htyang@iphy.ac.cn (H. Yang)

Abstract

The production of hydrogen by water electrolysis suffers from the kinetic barriers in the oxygen evolution reaction (OER) that limits the overall efficiency. As spin-dependent kinetics exist in OER, the spin alignment in active OER catalysts is critical for reducing the kinetic barriers in OER. It is effective to facilitate the spin polarization in ferromagnetic catalysts by applying external magnetic field, which increases the OER efficiency. However, more active OER catalysts tend to have dynamic open-shell orbital configurations with disordered magnetic moments, without showing an apparent long-range interatomic ferromagnetism; thus controlling the spin alignment of these active catalysts is challenging. In this work, we report a strategy with spin pinning effect to make the spins in active oxyhydroxides more aligned for higher intrinsic OER activity. Such strategy bases on a controllable reconstruction: ferromagnetic oxides with controlled sulfurization can evolve into stable oxide_{FM}/oxyhydroxide configurations with a thin oxyhydroxide layer under operando condition. The spin pinning effect is found at the interface of oxide_{FM}/oxyhydroxide. The spin pinning effect can promote spin selective electron transfer on OER intermediates to generate oxygens with parallel spin alignment, which facilitates the production of triplet oxygen and increases the intrinsic activity of oxyhydroxide by ~ 1 order of magnitude. Under spin pinning, the spins in oxyhydroxide can become more aligned after magnetization as long-range ferromagnetic ordering is established on the magnetic domains in oxide_{FM}. The OER kinetics are facilitated accordingly after magnetization, implying that the spin pinning effect is involved in the rate-determining step and this step is spin dependent. The spin polarization process in OER under spin pinning is also believed to be sensitive to the existence of active oxygen ligand (O(-)) in oxyhydroxide. When the O(-) is created in 1st deprotonation step under high pH, the spin polarization of ligand oxygens will be facilitated, which reduces the barrier for subsequent O-O coupling and promotes the O₂ turnover.

In the process of realizing the hydrogen energy infrastructure, the application and optimization of technologies like water electrolyzers is critical. One of essential tasks for such application is the development of robust and low-cost catalysts for the oxygen evolution reaction (OER), which gives the major energy loss in water electrolysis.¹⁻² Low-cost transition metal oxides (TMOs) are now intensively studied for efficient OER catalysis.^{1,3} In a variety of studies, some Co-based perovskites and spinels have been found to undergo operando reconstruction to form active Co (oxy)hydroxides in alkaline condition during OER.⁴⁻⁵ The di-μ-oxo bridged Co-Co sites in reconstructed (oxy)hydroxides induce the high OER activity after the deprotonation process, which generates the active oxygen ligand.⁶⁻⁷ More effort has been made to explore reconstructable oxides and many excellent pre-catalysts have been developed.⁸⁻⁹ According to current study, the Co (oxy)hydroxides have been revealed as actual active species in the most reconstructable Co-based oxides in alkaline OER. Thus, leading the Co (oxy)hydroxides toward higher OER activity is now a critical step for developing high-performing OER pre-catalysts.

On the other hand, on the basis of current knowledge of OER, the OER kinetics are spin dependent.¹⁰⁻¹² In OER, the reactants including OH⁻ and H₂O are singlet while the product oxygen has a triplet ground state with parallel spin alignment (↑ O = O ↑). The oxygen with triplet ground state was reported at a lower energy level of ~ 1 eV than its next excited state (the singlet oxygen).¹³ Thus, a spin polarization for producing triplet oxygen should be in a preferred path for good OER catalysts.¹⁴ Considering the spin conservation for fast kinetics, the spin alignment in Co (oxy)hydroxides is critical for facilitating the spin-dependent reactions in OER.¹⁰⁻¹¹ Note that for spin-dependent catalysis, spin-selection, spin-dependent electron mobility, spin-potentials in activation barriers could be optimized as Quantum Spin Exchange Interactions (QSEI) introduce a significant reduction of the electronic repulsions in the active d-orbitals of catalysts.¹⁵ The maximum kinetic rates occur at catalytic interfaces with dominant ferromagnetic (FM) electronic delocalization, $\Delta H_{\uparrow\downarrow\rightarrow\uparrow\uparrow}^{act.FM} = \Delta H_{\uparrow\downarrow\rightarrow\uparrow\uparrow}^{act.Non-Magnetic} - \Delta H_{\uparrow\downarrow\rightarrow\uparrow\uparrow}^{FM.QSEI}$, where $\Delta H_{\uparrow\downarrow\rightarrow\uparrow\uparrow}^{act.FM}$ is the activation enthalpy in a general spin selective step and $-\Delta H_{\uparrow\downarrow\rightarrow\uparrow\uparrow}^{FM.QSEI}$ can reduce the barriers because of QSEI.^{10, 12}

The understanding of the QSEI in catalysis is associated with the Goodenough-Kanamori rules that explain the dominant magnetic ordering observed in magnetic metal oxides.¹⁶ The dominant ferromagnetic orderings of ferromagnetic catalysts can be easily achieved as the magnetic moments in materials align along with the applied external magnetic field. A magnetic field-enhanced OER has been found recently in some ferromagnetic oxides,¹⁴ indicating the critical role of spin alignment in OER catalysis. It is also noted that some Co (oxy)hydroxides,¹⁷ especially for those evolving under *in-situ* OER condition,⁴ have been reported among the best non-noble metal based catalysts in alkaline media. For aligning the spins in Co (oxy)hydroxides, it should be noted that the Co

(oxy)hydroxides typically do not show extended ferromagnetism (FM) orderings,¹⁸⁻¹⁹ thus the need for extremely high operando magnetic field which would be rather difficult to apply in water electrolysis systems. Alternatively, for Co (oxy)hydroxide, it would be easier to control its spin alignment through a strong interaction in the interface between ferromagnetic materials and materials without long-range ferromagnetism, which is known as “spin pinning”.²⁰⁻²¹ It would come from the strong chemical bond in the interface of the two materials which creates a strong magnetic anisotropy field. At the interface, the atoms could form a unit spin system through a long-range exchange interaction.²² However, the spin pinning effect, toward enhanced OER catalysis, has not yet been demonstrated to our knowledge; and it is also challenging to realize the spin pinning in Co (oxy)hydroxide, especially difficult in reconstructable pre-catalysts.

Here, we report a high-performing oxide_{FM}/oxyhydroxide system where the spin pinning has been realized intrinsically in Co oxyhydroxide layer on ferromagnetic Co_xFe_{3-x}O₄ substrates (oxide_{FM}/oxyhydroxide). Under spin pinning effect, the spins can be further aligned after a short-time magnetization under magnetic field, which further increases the OER activity. The spin pinning effect benefits from a stable oxide_{FM}/oxyhydroxide interface and the long-range interaction is usually within 5 nm.^{20, 22} This calls for a stable oxide_{FM}/oxyhydroxide configuration and an oxyhydroxide layer with limited thickness. We have achieved such stable oxide_{FM}/oxyhydroxide configuration by a controllable reconstruction. The Co_xFe_{3-x}O₄ oxides with controlled sulfurization degree can undergo surface reconstruction under OER condition to evolve Co oxyhydroxides layer in limited thickness of ~ 4 nm. At the interface, FM magnetic domains in Co_xFe_{3-x}O₄ with highly aligned spins can result in a strong pinning of the spins in oxyhydroxide layer, for which the reconstructed oxyhydroxide exhibits higher intrinsic OER activity than directly prepared Co(Fe) oxyhydroxides by ~ 1 order of magnitude. After magnetization, the OER enhancement was notable only if the spin pinning had been established with ferromagnetic substrates, and its effect can be turned OFF by demagnetization. This implies that the spin pinning effect is involved in the rate-determining step (RDS) of OER, and the RDS also believed to be spin-related. Under spin pinning, the 2p electrons in reactant oxygens with specific spin state (spin up or spin down) can transfer through catalysts during OER process, which creates oxygens with parallel spin alignment and thus promoting the production of triplet oxygen ($\uparrow \text{O} = \text{O} \uparrow$). Besides, it is also believed that the involvement of the negatively charged active oxygen ligand with more unpaired non-bonding p electrons in reconstructed oxyhydroxide is critical for the spin polarization in OER. As the active oxygen ligands are created at the 1st deprotonation step, the spin polarization of oxygens can be facilitated accordingly under spin pinning, which reduces the barrier for the subsequent -O-O- coupling (RDS); otherwise to reach oxygen radicals with parallel spin

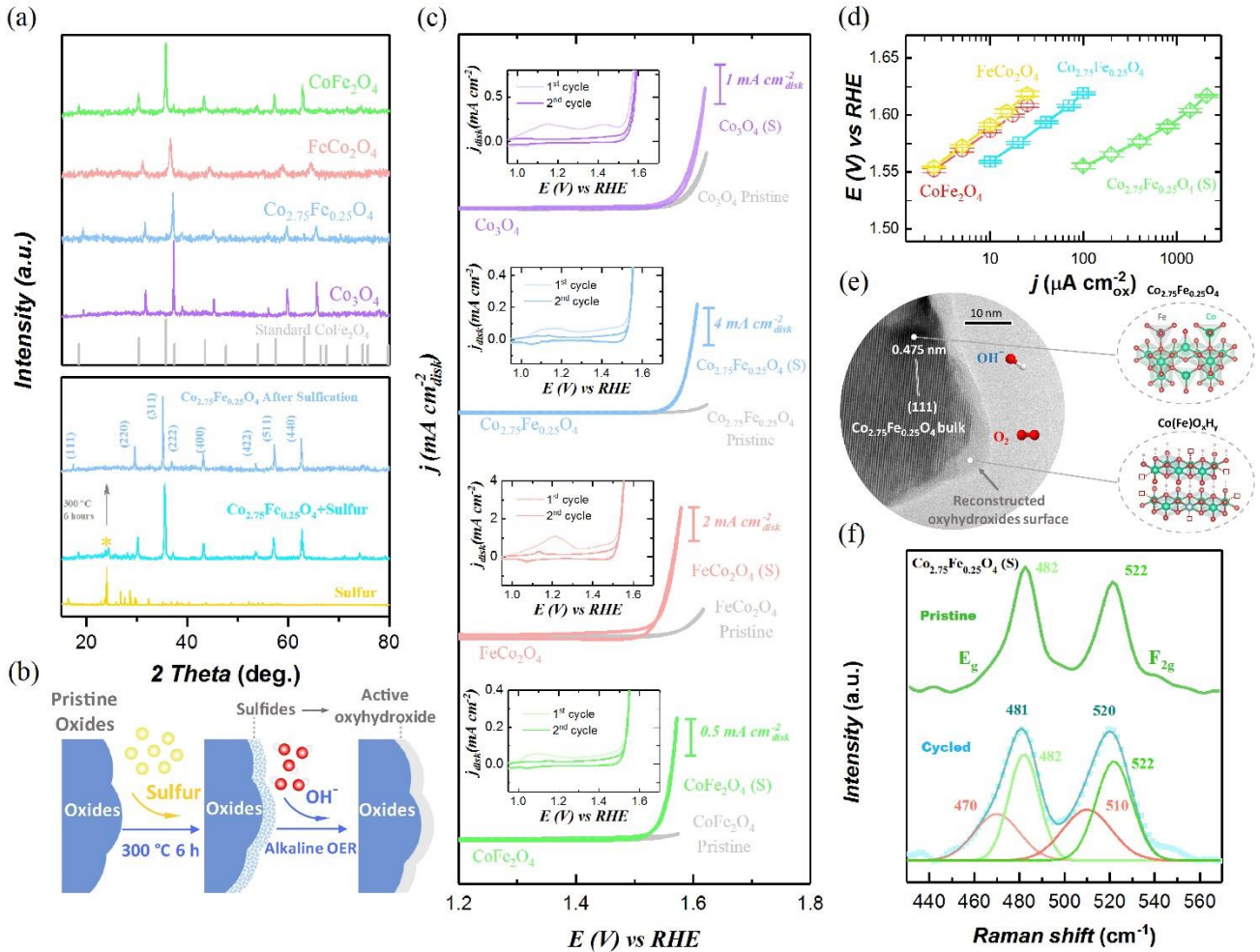
alignment after the 2nd deprotonation step will cause additional barrier before O₂ turnover. Overall, the design of oxide_{FM}/oxyhydroxide system bases on a controllable surface reconstruction and introduces spin pinning effect to enhance OER.

Result and discussion

Controllable surface reconstruction

The surface reconstruction of many catalysts under OER condition provides chances to enhance their OER performance as the surface oxyhydroxide species are evolved as the active sites for OER.^{4, 23-24} In the TMOs, the perovskite like Ba_{0.5}Sr_{0.5}Co_{0.8}Fe_{0.2}O_{3-δ} (BSCF) is well-known for its high specific activity and reconstructability under alkaline OER.^{1, 25-26} Such high reconstructability originates from a high oxygen p state, strong metal-oxygen covalency, and lattice oxygen participation in OER.⁵ The reconstructability can be even more notable in most metal chalcogenides, nitrides, and phosphides, which will undergo complete reconstruction to oxyhydroxide species under OER condition.²⁷ The alkaline reconstruction is a simple and effective way to generate highly active oxyhydroxide that could be applied in the spin pinning system. The pinning depth which is affected by the long-range exchange is usually within 5 nm and the pinning effect requires a stable oxide_{FM}/oxyhydroxide interface.^{20, 22} Thus, it is critical to design controllable surface reconstruction with finally stable surface chemistry and limited oxyhydroxide layer. Our design starts with Co_{3-x}Fe_xO₄ spinels which are stable during alkaline OER. The Co_{3-x}Fe_xO₄ (x=0~2.0) were synthesized by a sol-gel method. The top panel in Fig. 1a gives all powder X-ray diffraction (XRD) patterns of Co_{3-x}Fe_xO₄. As observed, the diffraction peaks in their XRD patterns match well with standard cubic spinel (Fd-3m), indicating pure-phase spinel structure of Co_{3-x}Fe_xO₄. Then, we performed low-degree sulfurization on Co_{3-x}Fe_xO₄ (the products denote as Co_{3-x}Fe_xO₄ (s)). A small amount of sulfur was mixed evenly with Co_{3-x}Fe_xO₄ powder, followed by heat treatment under 300 °C for 6 hours. As seen in the XRD patterns of Co_{2.75}Fe_{0.25}O₄ + sulfur before and after heat treatment (Bottom panel, Fig. 1a), the peaks attributed to sulfur disappear, which implies the completion of sulfurization. Please see details of sulfurization in the Method. The sulfurization degree is obtained according to the elemental ratio of Co_{3-x}Fe_xO₄ (s) by ICP-OES measurement and summarized in Supplementary Table 1. We assumed that the sulfurization would promote the reconstruction under OER. Indeed, as sulfur owns higher p state than oxygen and stronger M-S covalent bond than M-O,²⁸⁻²⁹ it is more reactive for lattice sulfur than lattice oxygen in OER, which grants great structural flexibility for reconstruction. Considering this, it is reasonable that many metal

139 sulfides were reported to undergo notable reconstruction into (oxy)hydroxides when serving as alkaline OER
 140 catalysts.³⁰ With the lattice sulfur at the surface of stable oxides, the reconstruction could be promoted at the surface
 141 and is under control by the sulfurization degree (Fig. 1b).



144
 145 **Fig. 1 | Controllable surface reconstruction on $\text{Co}_{3-x}\text{Fe}_x\text{O}_4$ spinel oxides for OER.** **a**, The powder X-ray diffraction
 146 (XRD) patterns of as-synthesized $\text{Co}_{3-x}\text{Fe}_x\text{O}_4$ ($x=0\sim2.0$) (top) and $\text{Co}_{2.75}\text{Fe}_{0.25}\text{O}_4$ as selected example before and after
 147 sulfurization (Bottom). **b**, The schematic diagram of a controllable reconstruction on oxides by controlling the
 148 sulfurization. The sulfurized products are denoted as $\text{Co}_{3-x}\text{Fe}_x\text{O}_4$ (s). **c**, The cyclic voltammetry (CV) curves of
 149 $\text{Co}_x\text{Fe}_{3-x}\text{O}_4$ ($x=0\sim2.0$) in O_2 saturated 1 M KOH with a scan rate of 10 mV s^{-1} . Inset is the 1st and 2nd CVs of sulfurized
 150 oxides (noted as $\text{Co}_{3-x}\text{Fe}_x\text{O}_4$ (s)). **d**, The Tafel plots of the OER specific activity of $\text{Co}_{2.75}\text{Fe}_{0.25}\text{O}_4$ (s) versus pristine
 151 $\text{Co}_{3-x}\text{Fe}_x\text{O}_4$ oxides. The plots are given after oxide surface area normalization, capacitance correction, and iR
 152 correction. The error bars represent the standard deviation from three independent measurements. **e**, The High-

Resolution Transmission Electron Microscope (HRTEM) image of $\text{Co}_{2.75}\text{Fe}_{0.25}\text{O}_4$ (s) after reconstruction (i.e. $\text{Co}_{2.75}\text{Fe}_{0.25}\text{O}_4/\text{Co}(\text{Fe})\text{O}_x\text{H}_y$). The HRTEM sample is from the electrode that was cycled without adding carbon. The bulk $\text{Co}_{2.75}\text{Fe}_{0.25}\text{O}_4$ oxide is covered by an amorphous (oxy)hydroxide layer with thickness of ~ 4 nm. **f**, The Raman spectra of $\text{Co}_{2.75}\text{Fe}_{0.25}\text{O}_4$ (s) before and after operating under OER. The peaks at Raman shift of 482 and 522 cm^{-1} are assigned to E_g and F_{2g} mode in $\text{Co}_{2.75}\text{Fe}_{0.25}\text{O}_4$ spinel. The broad peaks at Raman shift of 470 and 510 cm^{-1} are resulted by the bending and stretching of O-Co-O in amorphous $\text{Co}(\text{Fe})\text{O}_x\text{H}_y$.³¹⁻³³

Our electrochemical results support this hypothesis. Fig. 1c shows the cyclic voltammetry (CV, 2nd cycle) curves of $\text{Co}_x\text{Fe}_{3-x}\text{O}_4$ (s) and pristine $\text{Co}_x\text{Fe}_{3-x}\text{O}_4$ in 1 M KOH (please see details for measurements in Method). The inset panels exhibit the 1st and 2nd CV cycles of $\text{Co}_x\text{Fe}_{3-x}\text{O}_4$ (s). It was found that the $\text{Co}_x\text{Fe}_{3-x}\text{O}_4$ (s) with low-degree sulfurization exhibit much larger pseudocapacitance in the 1st cycle than in the 2nd cycle, indicating notable reconstruction in 1st cycle. Such reconstruction is, however, negligible on pristine $\text{Co}_x\text{Fe}_{3-x}\text{O}_4$ (Supplementary Fig. 1). Without sulfurization, the pristine $\text{Co}_x\text{Fe}_{3-x}\text{O}_4$ (e.g. CoFe_2O_4) could survive for at least 500 CVs in 1 M KOH with negligible surface reconstruction under the observation by HRTEM (Supplementary Fig. 2a and 2b). The reconstruction of oxides after sulfurization is further investigated using the sulfurized $\text{Co}_{2.75}\text{Fe}_{0.25}\text{O}_4$ with different sulfurization degrees (see details in Supplementary Note 1). Hence, we believe a low-level sulfurization would be effective to control the surface reconstruction of oxides. After reconstruction, $\text{Co}_x\text{Fe}_{3-x}\text{O}_4$ (s) deliver much higher activity than pristine $\text{Co}_x\text{Fe}_{3-x}\text{O}_4$ oxides (Fig. 1c). By evolving the $\text{Co}(\text{Fe})\text{O}_x\text{H}_y$ surface from the pristine materials of $\text{Co}_{2.75}\text{Fe}_{0.25}\text{O}_4$ (s), FeCo_2O_4 (s) and CoFe_2O_4 (s), the activity increment after reconstruction is notable (more than 20 times at overpotential of 350 mV). However, for pure Co_3O_4 without Fe involvement, the activity increase after reconstruction is about 2 times at overpotential of 350 mV. Thus, Fe component plays an important role in reconstructed oxyhydroxide, which is previously reported to promote the deprotonation process to generate active oxygen ligand, thus boosting the OER performance.⁹ Overall, we have shown that the low degree sulfurization is a simple but effective strategy for promoting the reconstruction of $\text{Co}_x\text{Fe}_{3-x}\text{O}_4$ oxides during alkaline OER. By adjusting the elemental ratio in pre-catalysts (like the ratio of Co, Fe in our case), the activity of reconstructed oxyhydroxide could be optimized. In $\text{Co}_x\text{Fe}_{3-x}\text{O}_4$ (s), $\text{Co}_{2.75}\text{Fe}_{0.25}\text{O}_4$ (s) exhibits highest specific OER activity after reconstruction (Supplementary Fig. 6). The activity $\text{Co}_{2.75}\text{Fe}_{0.25}\text{O}_4$ (s) with and without mixing carbon is also examined (Supplementary Fig. 7a and 7b). Without carbon, the $\text{Co}_{2.75}\text{Fe}_{0.25}\text{O}_4$ (s) after reconstruction still exhibited good performance, indicating its potential for practical applications. The specific OER activity of $\text{Co}_{2.75}\text{Fe}_{0.25}\text{O}_4$ (s) in Tafel plots is compared to pristine $\text{Co}_x\text{Fe}_{3-x}\text{O}_4$ oxides in Fig. 1d. The current density

has been normalized to oxide surface area which is determined by Brunauer-Emmett-Teller (BET) measurements (Supplementary Fig. 8).³⁴ In Tafel plots, the specific activity of $\text{Co}_{2.75}\text{Fe}_{0.25}\text{O}_4$ (s) is superior to that of all pristine $\text{Co}_x\text{Fe}_{3-x}\text{O}_4$. Note that we are able to get specific activity by normalizing current density to oxide surface area³⁵ because we have controlled the reconstruction strictly on surface with limited depth. This is evidenced by investigating the reconstructed $\text{Co}_{2.75}\text{Fe}_{0.25}\text{O}_4$ (s) under high resolution transmission microscopy (HRTEM). In the HRTEM image of $\text{Co}_{2.75}\text{Fe}_{0.25}\text{O}_4$ (s) after 20 cycles (Fig. 1e), we observed an amorphous oxyhydroxide surface with uniform thickness of ~ 4 nm on $\text{Co}_{2.75}\text{Fe}_{0.25}\text{O}_4$ bulk. The Raman spectra of $\text{Co}_{2.75}\text{Fe}_{0.25}\text{O}_4$ (s) before and after cycling are also presented in Fig. 1f. In top curve, two peaks at Raman shift of 482 and 522 cm^{-1} are assigned to E_g and F_{2g} mode in pristine $\text{Co}_{2.75}\text{Fe}_{0.25}\text{O}_4$ spinel.³⁶ After cycling (bottom curve), these two peaks are broadened and with lower Raman shift, which is resulted by additional features of bending and stretching of O-Co-O in amorphous $\text{Co}(\text{Fe})\text{O}_x\text{H}_y$ (at 470 and 510 cm^{-1})³¹⁻³³. The controllable reconstruction with limited oxyhydroxide layer still brings remarkable activity enhancement because the electrochemical reactions are sensitive to surface chemistry. In another word, the reconstructed oxyhydroxides layer with limited thickness are efficiently used for OER enhancement but not compromising the bulk stability. This also meets the need to reach a stable oxide_{FM} /oxyhydroxide configuration for realizing spin pinning effect.

Spin pinning effect toward OER enhancement

By controlling a low-level sulfurization of pre-catalysts, we have successfully realized a stable oxyhydroxide surface with limited thickness (~ 4 nm) on ferromagnetic $\text{Co}_{3-x}\text{Fe}_x\text{O}_4$ oxides (oxide_{FM} /oxyhydroxide) under alkaline OER. To study the spin pinning effect in $\text{Co}_{3-x}\text{Fe}_x\text{O}_4/\text{Co}(\text{Fe})\text{O}_x\text{H}_y$, the intrinsic OER activity of the reconstructed $\text{Co}(\text{Fe})\text{O}_x\text{H}_y$ was studied. The turnover frequency (TOF) of $\text{Co}_{2.75}\text{Fe}_{0.25}\text{O}_4/\text{Co}(\text{Fe})\text{O}_x\text{H}_y$ is shown in Fig. 2a, in comparison with the directly prepared $\text{Co}(\text{Fe})$ oxyhydroxides (one synthesized by us and one benchmark reported in literature; the Co/Fe ratio in oxyhydroxides is close to that in $\text{Co}_{2.75}\text{Fe}_{0.25}\text{O}_4$). The bottom bound refers to the TOF by assuming all metal cations in the catalyst are effective (denoted as “bulk”) and the upper one refers to the TOF by calculating only the active metal cations on the surface (denoted as “surface”). The details about the TOF evaluation are given in Method part. The details about the synthesis and characterizations of $\text{Co}_{0.9}\text{Fe}_{0.1}\text{OOH}$ are provided in Supplementary Note 2. The as-synthesized $\text{Co}_{0.9}\text{Fe}_{0.1}\text{OOH}$ shows comparable $\text{TOF}_{\text{surface}}$ value with the benchmark $\text{Co}_{0.86}\text{Fe}_{0.14}(\text{OOH})$. Notably, the reconstructed $\text{Co}(\text{Fe})\text{O}_x\text{H}_y$ exhibits $\text{TOF}_{\text{surface}}$ of ~ 1 order of magnitude greater than pure $\text{Co}(\text{Fe})$ oxyhydroxide at 1.58 V (overpotential of 350 mV). The OER specific current densities of

211 $\text{Co}_{2.75}\text{Fe}_{0.25}\text{O}_4/\text{Co}(\text{Fe})\text{O}_x\text{H}_y$ and $\text{Co}_{0.9}\text{Fe}_{0.1}\text{OOH}$ (normalized to the BET surface area) are shown in Tafel plots
212 (Supplementary Fig. 10). It is consistently to find that the $\text{Co}_{2.75}\text{Fe}_{0.25}\text{O}_4/\text{Co}(\text{Fe})\text{O}_x\text{H}_y$ delivers higher specific activity
213 (~ 1 order of magnitude) than $\text{Co}_{0.9}\text{Fe}_{0.1}\text{OOH}$ at ~ 1.58 V. In addition, as compared with other well-known state-of-
214 art OER catalysts, the TOF of $\text{Co}_{2.75}\text{Fe}_{0.25}\text{O}_4/\text{Co}(\text{Fe})\text{O}_x\text{H}_y$ on a per-surface-site basis is among the highest reported to
215 date for alkaline OER catalysts.

216

217 To substantially evidence the spin pinning effect, we measured the magnetism of the reconstructed CoFe_2O_4 (s) (i.e.
218 $\text{CoFe}_2\text{O}_4/\text{Co}(\text{Fe})\text{O}_x\text{H}_y$) and the pristine CoFe_2O_4 under both field-cooled (FC) mode and zero-field-cooled (ZFC)
219 mode. The magnetic hysteresis loops are shown in Fig. 2b and Supplementary Fig. 11. In the hysteresis loop of
220 $\text{CoFe}_2\text{O}_4/\text{Co}(\text{Fe})\text{O}_x\text{H}_y$, it exhibits large coercivity (H_C) and a notable magnetization switching behavior at around
221 zero field under both FC and ZFC modes.³⁷⁻³⁸ However, the magnetization switching behavior is negligible for
222 pristine CoFe_2O_4 while the high H_C is still notable. For $\text{CoFe}_2\text{O}_4/\text{Co}(\text{Fe})\text{O}_x\text{H}_y$, the notable magnetization switching
223 behavior at around zero field indicates that the CoFe_2O_4 substrate and the $\text{Co}(\text{Fe})\text{O}_x\text{H}_y$ layer exhibit different
224 magnetic properties, and the CoFe_2O_4 substrate serves as a strong ferromagnet leading to a high H_C . Moreover, the
225 loop of $\text{CoFe}_2\text{O}_4/\text{Co}(\text{Fe})\text{O}_x\text{H}_y$, under FC mode, exhibits up and left shift compared to that under ZFC mode, while
226 nearly no shift is observed in the hysteresis loop of pristine CoFe_2O_4 . The up and left shift of $\text{CoFe}_2\text{O}_4/\text{Co}(\text{Fe})\text{O}_x\text{H}_y$
227 under FC mode indicates an exchange bias effect that originates from uncompensated interfacial spins that are pinned
228 in the oxyhydroxide layer and do not follow the external magnetic field (Fig. 2c).³⁹⁻⁴⁰ Such pinning effect is intrinsic.
229 Under the electrochemical condition, the spin pinning can well persist. 72-hour chronopotentiometry test was
230 performed on $\text{Co}_{2.75}\text{Fe}_{0.25}\text{O}_4/\text{Co}(\text{Fe})\text{O}_x\text{H}_y$ under OER condition, in which only limited activity drop is found
231 (Supplementary Fig. 12a). The CVs before and after 72-hour chronopotentiometry test show negligible difference
232 (Supplementary Fig. 12b). CV cycling was also performed on $\text{Co}_{2.75}\text{Fe}_{0.25}\text{O}_4/\text{Co}(\text{Fe})\text{O}_x\text{H}_y$ and $\text{Co}_{2.75}\text{Fe}_{0.25}\text{O}_4$ for 500
233 cycles in 1 M KOH (Supplementary Fig. 13a-13d). The samples exhibit limited change since the 2nd cycle during
234 500 CV cycles. Note that the 1st cycle involves the reconstruction from the pre-catalyst (sulfurized $\text{Co}_{2.75}\text{Fe}_{0.25}\text{O}_4$) to
235 the desired catalyst ($\text{Co}_{2.75}\text{Fe}_{0.25}\text{O}_4/\text{Co}(\text{Fe})\text{O}_x\text{H}_y$) and thus its CV profile is different from other subsequent cycles. In
236 the Supplementary Fig. 14, HRTEM was conducted on the $\text{Co}_{2.75}\text{Fe}_{0.25}\text{O}_4/\text{Co}(\text{Fe})\text{O}_x\text{H}_y$ after 500 CV cycles. The
237 thickness of the oxyhydroxide layer still persisted its thickness after cycling. The thickness of the oxyhydroxide
238 surface layer remained unchanged and thus the interface pinning effect should not be affected, which is consistent
239 with the measured magnetic property. In Supplementary Fig. 15, the magnetic hysteresis loops of

CoFe₂O₄/Co(Fe)O_xH_y after 20 and 500 CV cycles show limited difference. The bias of hysteresis loop for the sample after 500 CV cycles still kept at ~1000 Oe. The evidence shows that the spin pinning persists in Co_{3-x}Fe_xO₄/Co(Fe)O_xH_y under the OER condition.

The intrinsic spin pinning effect led by the strong interface magnetic anisotropy originates from the existence of localized magnetic domains in the ferromagnetic substrate. In each magnetic domain, the spins are highly aligned (nearly 100%) through exchange effects, which is well known as “spontaneous magnetization” for ferromagnetism. The spin pinning usually happens when the magnetic domains are covered by compositions with disordered spins,²¹ and the spin pinning effect could be found at the interface (Supplementary Fig. 16).⁴¹⁻⁴² Such pinning effect establishes under long-range exchange effect. Thus, when the oxyhydroxide layer is thin enough (at ~ 4-5 nm), the spins of the whole layer can be aligned by the underlying magnetic domains in the ferromagnetic substrate. This is the case of our findings in the Co_{3-x}Fe_xO₄/Co(Fe)O_xH_y, in which the Co_{3-x}Fe_xO₄ is ferromagnetic and the paramagnetic Co(Fe)O_xH_y is a thin layer. The spins in reconstructed Co(Fe)O_xH_y will be affected by a strong interface magnetic anisotropy and follow the spin ordering in the localized magnetic domains (Fig. 2d, left). However, not all magnetic domains in the ferromagnetic materials are completely aligned in nature. That makes the spins in Co(Fe)O_xH_y only aligned in part on the surface of localized magnetic domains before magnetization. After magnetization, nearly all magnetic domains can be aligned to establish a long-range ferromagnetic (FM) ordering, which makes the spins in Co(Fe)O_xH_y become completely aligned along with the FM ordering (Fig. 2d, right). The spin ordering in the paramagnetic surface layer is thus further improved by magnetization.

It was then examined if the enhanced spin alignment can further improve the OER. We performed OER linear sweep voltammetry (LSV) of Co_{3-x}Fe_xO₄ (s) after following three procedures, respectively: 1. after the complete surface reconstruction; 2. after the magnetization under a magnetic field of 0.5 T for 15 min and then removal of the magnetic field; 3. after the post-treatment under 120 °C for 1 min. The results are shown in Fig. 2e. We also measured the magnetization curves of all substrate oxides (Co_{3-x}Fe_xO₄) as shown in Fig. 2f. As seen in Fig. 2e, for reconstructed Co_{3-x}Fe_xO₄ (s) (i.e. Co_{3-x}Fe_xO₄/Co(Fe)O_xH_y), their OER performance can be further improved after magnetization with ferromagnetic substrates like Co_{2.75}Fe_{0.25}O₄, FeCo₂O₄, and CoFe₂O₄. However, with Co₃O₄ substrate, which is paramagnetic at room temperature,⁴³ there is no activity enhancement after magnetization. It demonstrates that the magnetization can affect the OER efficiency of reconstructed oxyhydroxide surface layer only if the spin pinning

was established by using a ferromagnetic substrate. Besides, the activity enhancement for catalysts with $\text{Co}_{2.75}\text{Fe}_{0.25}\text{O}_4$, FeCo_2O_4 , and CoFe_2O_4 substrates are also different. In Fig. 2a, the grey dash lines denote the OER potential where the current density has been improved by 20% compared to that before magnetization. For $\text{Co}_{2.75}\text{Fe}_{0.25}\text{O}_4$, such improvement is observed at an OER potential of 1.60 V vs. RHE while for FeCo_2O_4 and CoFe_2O_4 with higher magnetization than $\text{Co}_{2.75}\text{Fe}_{0.25}\text{O}_4$, such improvement has already been notable at lower potential (1.53 V vs. RHE). Such activity enhancement strongly depends on the magnetization of $\text{Co}_{3-x}\text{Fe}_x\text{O}_4$ substrate. To further confirm the observed OER enhancement, the Tafel plots using steady current by chronoamperometric (CA) test were conducted (Supplementary Fig. 18a and 18b). The result is consistent with those from LSV tests and the OER enhancement after magnetization is notable.

278

To check if the enhancement of OER current density was simply resulted by the decrease of electrical resistivity of the oxide after magnetization. The CoFe_2O_4 with the highest ferromagnetism among these oxides was tested for its magnetoresistance (Supplementary Fig. 19). Consistent with what has been previously reported for CoFe_2O_4 ,⁴⁴ it shows very limited change of the magnetoresistance after being magnetized under 0.5 T for 15 min. Further, a ferromagnetic metal/oxyhydroxide configuration is constructed by cycling the Ni foil in 1 M KOH (Supplementary Fig. 20a-20b). The activity enhancement of Ni foil can be observed after magnetization, and such activity enhancement by magnetization diminished after demagnetization (Supplementary Fig. 20c). As the Ni metal own high conductivity, the magneto-resistive effect can be excluded from the observed OER enhancement after the magnetization of metal/oxyhydroxide configuration. Moreover, it is also examined if other electrochemical oxidation reactions in alkaline media such as methanol oxidation reaction (MOR) and formic acid oxidation reaction (FOR) can be enhanced by magnetizing the $\text{CoFe}_2\text{O}_4/\text{Co}(\text{Fe})\text{O}_x\text{H}_y$ electrode (Supplementary Fig. 21a -21d). If the OER activity enhancement by magnetization is resulted by magneto-resistive effect, the similar activity increase should be found in MOR and FOR as well. However, none of these reactions can be found with enhanced activity after magnetization. Other possible reasons for the activity enhancement by magnetization are also examined and excluded as discussed in Supplementary Note 3. Therefore, we believe that the magnetoresistance is not responsible for the observed OER enhancement. That OER shows unique activity enhancement by magnetization should be ascribed to unique OER steps (spin-related) from singlet reactant to the triplet product ($\uparrow \text{O} = \text{O} \uparrow$).

296

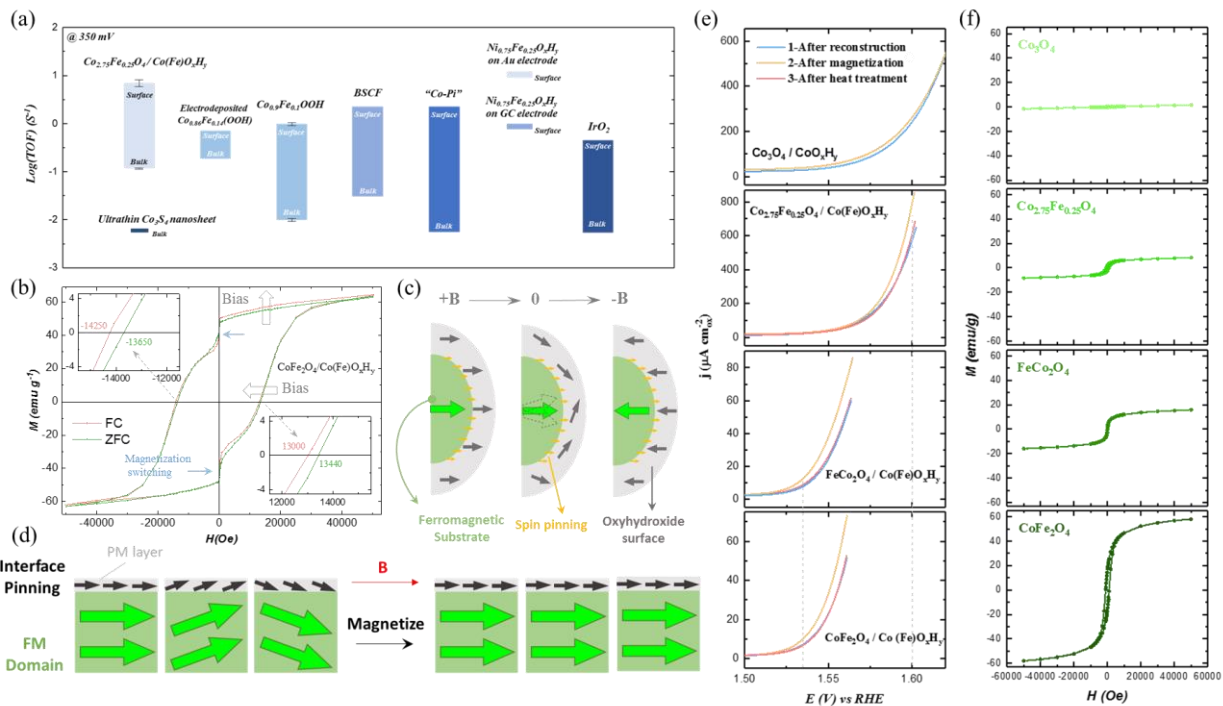


Fig. 2 | OER enhancement by spin pinning in $\text{Co}_{3-x}\text{Fe}_x\text{O}_4/\text{Co}(\text{Fe})\text{O}_x\text{H}_y$ under magnetic field. **a**, Turnover frequency (TOF) values of reconstructed $\text{Co}_{2.75}\text{Fe}_{0.25}\text{O}_4(\text{s})$ (i.e. $\text{Co}_{2.75}\text{Fe}_{0.25}\text{O}_4 / \text{Co}(\text{Fe})\text{O}_x\text{H}_y$), electrodeposited $\text{Co}_{0.88}\text{Fe}_{0.12}(\text{OOH})$,¹⁷ $\text{Co}_{0.9}\text{Fe}_{0.1}\text{OOH}$, $\text{Ba}_{0.5}\text{Sr}_{0.5}\text{Co}_{0.8}\text{Fe}_{0.2}\text{O}_{3-6}$ (BSCF) film,⁴⁵⁻⁴⁶ electrodeposited cobalt hydroxide ("Co-Pi"),⁴⁶⁻⁴⁷ $\text{Ni}_{0.75}\text{Fe}_{0.25}\text{O}_x\text{H}_y$ NPs on Au electrode,⁴⁸ electrodeposited $\text{Ni}_{0.75}\text{Fe}_{0.25}\text{O}_x\text{H}_y$ on glassy carbon (GC) electrode⁴⁹, IrO_2 (in acid)⁵⁰ and ultrathin Co_3S_4 nanosheet⁵¹. The TOF_{bulk} and $\text{TOF}_{\text{surface}}$ of some catalysts present the lower and upper limits of the estimated TOF for fair comparison. The methods for TOF evaluation are given in Method part. **b**, The magnetic hysteresis loops of CoFe_2O_4 (s) after 10 OER CVs (i.e. $\text{CoFe}_2\text{O}_4/\text{Co}(\text{Fe})\text{O}_x\text{H}_y$) under both field-cooled (FC) mode and zero-field-cooled (ZFC) mode. The inset provides enlarged panels showing the loops that intersect with $y=0$ axis. **c**, The schematics of the exchange bias under switching magnetic field, which is closely associated with the spin pinning effect at the interface of ferromagnetic substrate/oxyhydroxide. **d**, The schematic illustration of the spin pinning effect at the interface between ferromagnetic (FM) magnetic domains and the thin paramagnetic (PM) oxyhydroxide layer, and the spins in the PM oxyhydroxide layer can be aligned more under magnetization. **e**, Linear sweep voltammetry (LSV) of $\text{Co}_{3-x}\text{Fe}_x\text{O}_4$ (s) after reconstruction in 1 M KOH following the procedures: 1. After reconstruction (10 CV cycles in 1 M KOH, light blue), 2. After magnetization under 0.5 T for 15 min and the removal of the magnetic field (yellow) and 3. After the post-treatment at 120 °C for 1 min (pinkish). The grey dash lines denote the OER potential where the current density has been improved by 20% compared to that before magnetization. The error bars represent the standard deviation from three independent

measurements are given in Supplementary Fig. 17. **f**, Magnetic hysteresis loops of $\text{Co}_{3-x}\text{Fe}_x\text{O}_4$ oxides.

The magnetization improves the spin polarization in materials, which was previously reported to positively affect OER.¹⁴ However, it is different in our case because the enhancement was observed after the magnetization, instead of in the presence of the external field. This is because the induced spin alignment by magnetization persisted for long even after the magnetic field was removed, which could be credited to the stable magnetization of ferromagnetic substrate when magnetic field was removed (Supplementary Fig. 22)⁵². The OER enhancement of $\text{CoFe}_2\text{O}_4/\text{Co}(\text{Fe})\text{O}_x\text{H}_y$ could preserve well in alkaline electrolyte for more than 2 hours, as evidenced by the LSV result in Supplementary Fig. 23a. The induced magnetization completely relaxed finally and the OER activity of $\text{CoFe}_2\text{O}_4/\text{Co}(\text{Fe})\text{O}_x\text{H}_y$ recovered to that before magnetization after overnight holding. But it should be noted that the catalysts still can be re-activated by magnetization again (Supplementary Fig. 23b). Besides, when the electrodes were heated at 120 °C for 1 min, the activity enhancement by magnetization soon diminished as the magnetic domains in $\text{Co}_{3-x}\text{Fe}_x\text{O}_4$ become disordered by thermal disturbance, and the OER activity of $\text{Co}_{3-x}\text{Fe}_x\text{O}_4/\text{Co}(\text{Fe})\text{O}_x\text{H}_y$ returns to that before magnetization (Fig. 2e, pinkish lines). Overall, the turning ON/OFF the effect of magnetization and its sensitivity to ferromagnetic substrate demonstrate that the spin pinning effect indeed exists between the ferromagnetic of $\text{Co}_{3-x}\text{Fe}_x\text{O}_4$ substrate and the paramagnetic $\text{Co}(\text{Fe})\text{O}_x\text{H}_y$ surface layer.

Spin electrons in triplet oxygen production

In oxygen evolution reaction, the reactants including OH^- and H_2O are singlet while the product O_2 has a triplet ground state; the singlet excited state of O_2 is about 1 eV above the ground state.¹³ The OER for producing triplet oxygen from singlet OH^- or H_2O calls for a “spin selective” electron transfer. In non-magnetic catalysts, the appropriate addition of spin-dependent potentials at the catalytic interphase would accelerate the kinetics and reduce the over-potentials through enhanced QSEI spin-transfer.¹⁰ In our case, the spin pinning effect acts to create intrinsic channels for the polarization of spin electrons within the catalysts. Schematics illustrating the spin pinning effect toward producing triplet oxygen are presented in Fig. 3a and Fig. 3b in a simple way. As shown in Fig. 3a, spin-up and spin-down electrons are paired in the p state of oxygen in singlet OH^- and H_2O . The spins in substrate without ferromagnetism are originally unaligned. Thus, both spin-up and spin-down electrons are allowed to transfer. However, when spins are aligned (spin-up) and pinned in oxyhydroxide by ferromagnetic substrate, only spin-down electrons are allowed to pair with the spin-up electrons in oxyhydroxide. Such selective process under spin pinning

would promote a spin polarization in OER process to facilitate the generation of triplet oxygen ($\uparrow \text{O} = \text{O} \uparrow$). As shown in Fig. 3b, the OER process involve four-electron-transfer steps, in which unpaired O 2p electrons can be created at 1st and 3rd step. There are two possible paths (Path 1 and Path 2) to reach the Co-OO intermediate, depending on the spin electrons in oxygen p state. Path 1 will lead to a final production of triplet oxygen at lower energy of 1.1 eV than that of Path 2 for singlet oxygen, as revealed by our DFT study (Supplementary Fig. 24). Thus, for Path 2, the kinetics would be mostly blocked due to a high energy barrier required to give singlet oxygen.⁵³ For spin-unaligned substrate, the OER reactants take both Path 1 and Path 2 without spin selection, where the part of kinetics through Path 2 are blocked, and additional overpotential for spin polarization is required before the O₂ turnover. However, for Co_{3-x}Fe_xO₄/Co(Fe)O_xH_y with spins aligned and pinned, the Path 1 for producing triplet oxygen is much preferred, which leads to lower kinetic barrier for O-O coupling. Thus, the OER enhancement of Co_{3-x}Fe_xO₄/Co(Fe)O_xH_y by spin pinning effect is closely associated with the facilitated spin polarization for triplet oxygen production.

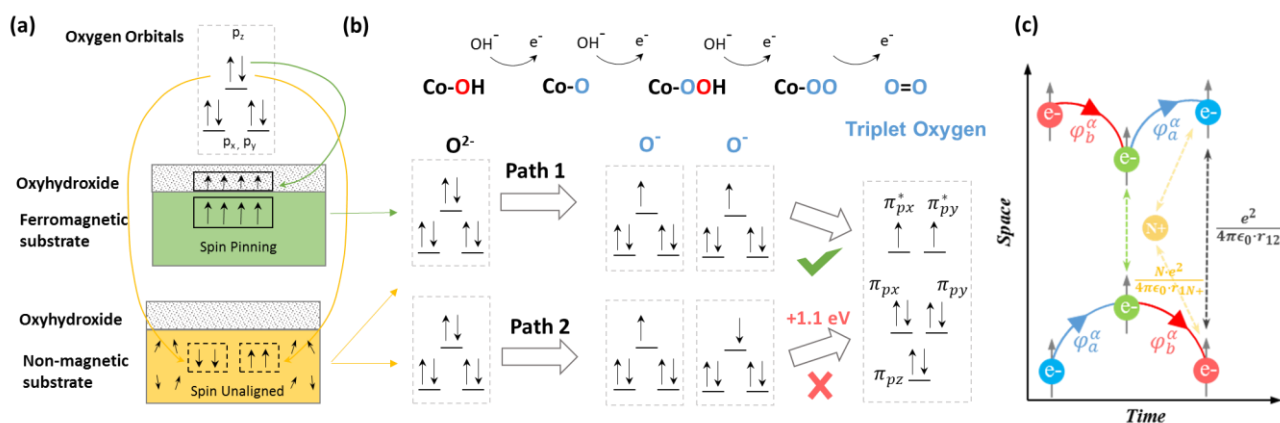


Fig. 3 | Spin pinning effect for triplet oxygen evolution on the oxyhydroxide. a, The spin-electron transfer from singlet oxygen (OH⁻, H₂O) to Co_{3-x}Fe_xO₄/Co(Fe)O_xH_y with and without spin pinning effect. **b**, The triplet oxygen production along with four-electron transfer process of OER. **c**, The QSEI mechanism in a space-time Feynman diagrams. Two electrons with the same spin approach, in time from the left side, to avoid the increase of the Coulomb repulsions the electrons exchange their orbitals (momentum) to effectively keep them apart. φ is the wavefunction of the orbitals (momentum) of spin electrons. The electronic repulsion between spin electrons is given as $\frac{e^2}{4\pi\epsilon_0 \cdot r_{12}}$ and electron-nuclei Coulomb attraction is given as $\frac{N \cdot e^2}{4\pi\epsilon_0 \cdot r_{1N+}}$.⁵⁴

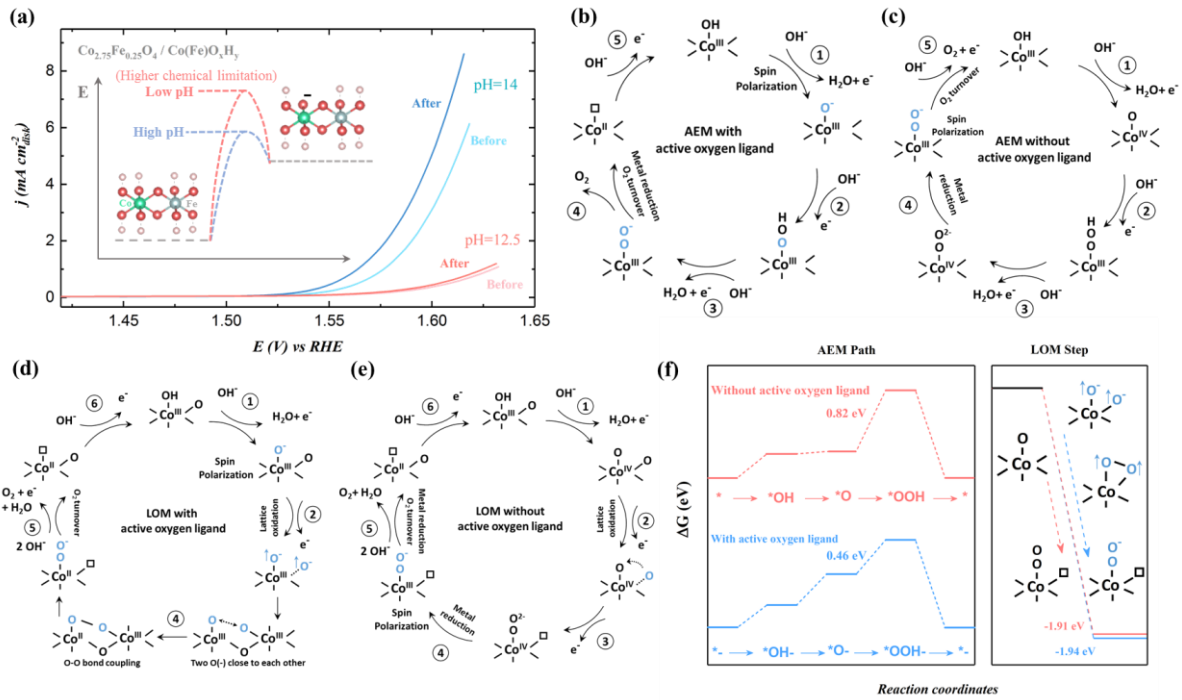
Our analysis may also explain recent findings of OER enhancement by directly applying magnetic field on some ferromagnetic oxides under operando condition.¹⁴ It should be noted here the significant role of long-range FM orderings toward OER catalysis. In spin-aligned systems, the inter-atomic electronic repulsions between spin-oriented electrons will decrease to optimize the QSEI spin-potentials. We show space-time Feynman diagrams in Fig. 3c to visualize the meaning of QSEI spin-potentials. When two electrons with the same spin at some point in time approaching each other (left side of Fig. 3c), to avoid the increase of the Coulomb repulsion, quantum mechanics allows only for electrons with the same spin to exchange their orbitals (momentum) to effectively keep them apart. As the right side of Fig. 3c shows, QSEI represent mechanisms that reduce the electronic repulsions, but also imply a decrease of the electron-nuclei Coulomb attractions. Catalysts with dominant cooperative ferromagnetic interactions, with an excess of degenerate empty valence orbitals, are stabilized via inter-atomic QSEI. The reduction of the electronic repulsions, dominant over Coulomb attractions, enhance the stabilization of electrons in the orbitals, also associated with extended spin mobility in dominant FM orderings. In relation with typical concepts in catalysis, QSEI make the stable $\text{Co}_{3-x}\text{Fe}_x\text{O}_4/\text{Co}(\text{Fe})\text{O}_x\text{H}_y$ catalytic interfaces to be more noble like, optimizing the spin-polarized kinetics.¹²

pH-dependent OER enhancement by spin pinning

We further investigated the OER enhancement by magnetization in alkaline media of different pH. Fig. 4a shows the LSV of reconstructed $\text{Co}_{2.75}\text{Fe}_{0.25}\text{O}_4$ (s) (i.e. $\text{Co}_{2.75}\text{Fe}_{0.25}\text{O}_4/\text{Co}(\text{Fe})\text{O}_x\text{H}_y$) before and after magnetization under pH of 12.5 and 14. It is clear that OER enhancement by magnetization is pH dependent. The influence of the resistance difference in the electrolytes with different pH has been excluded by iR-correction (Supplementary Fig. 25). The OER enhancement after magnetization is notable when performing OER in electrolyte of pH=14, while such enhancement becomes much limited in electrolyte of pH=12.5. In earlier study on Co oxyhydroxide, Fe component will induce the active oxygen species in oxyhydroxide by promoting the deprotonation of OH ligand.^{9, 55} The deprotonation of OH ligand can sometimes proceed in a non-concerted/decoupled way.⁵⁶ When the proton abstraction is not compensated by the metal oxidation but by a negatively charged oxygen ligand (proton deficient), the active oxygen ligand is created. Such deprotonation of -OH ligand to create active oxygen ligand can easily occur at high pH, while experiencing chemical limitations at low pH (inset of Fig. 4a).⁵⁵ No remarkable OER enhancement after magnetization at low pH would be associated with the difficulty in deprotonation of -OH ligand to create -O(-) under low-pH, and the negatively charged active oxygen ligand may critical for the spin polarization of oxygen radicals in

395 OER.

396



397

398 **Fig. 4 | Active lattice oxygen participation for producing triplet oxygen.** **a**, The linear sweep voltammetry (LSV)
 399 of the reconstructed $\text{Co}_{2.75}\text{Fe}_{0.25}\text{O}_4$ (s) (cycled in 1M KOH for 10 cycles to evolved $\text{Co}_{2.75}\text{Fe}_{0.25}\text{O}_4/\text{Co(Fe)O}_x\text{H}_y$)
 400 before and after magnetization in magnetic field of 0.5 T for 15 min under pH of 12.5 and 14. The inset is a schematic
 401 illustration of deprotonation under different pH for generating negatively charged oxygen on Co site. **b**, **c**, The
 402 adsorbate evolution mechanism (AEM) OER pathway for the spin polarization mechanism (b) with and (c) without
 403 active oxygen ligand (O^-) induced in the first electron transfer step. The early spin polarization mechanism is closely
 404 associated with the creation of O^- . **d**, **e**, The LOM OER pathway for the spin polarization mechanism (d) with and (e)
 405 without O^- . **d**, The Free energy diagram of OER at 1.23 V (vs. RHE) with and without the Fe-triggered active oxygen
 406 ligand on $\beta\text{-Co(OOH)}$ (001) slabs toward triplet oxygen production. The AEM pathway and LOM step are illustrated
 407 in left panel and right panel, respectively.

408

409 It is noticed that the OER performance of $\text{Co}_{2.75}\text{Fe}_{0.25}\text{O}_4/\text{Co(Fe)O}_x\text{H}_y$ is also pH dependent, which could be resulted
 410 by decoupled or non-concerted electron/proton transfer such as lattice oxygen-mediated mechanism (LOM).^{25, 57-58}
 411 It should be noted here that such electron/proton transfer may not be restricted to the LOM pathway, and it can also
 412 be involved in other OER steps. We then discuss the spin polarization of the ligand oxygen in OER pathways under

both AEM and LOM (Fig. 4b-4e). In the OER steps with AEM, the electron would transfer first from a metal center after the deprotonation of -OH, which is assigned to the redox of the metal center, like $\text{Co}^{\text{III}}/\text{Co}^{\text{IV}}$. However, in the cases with active oxygen ligand, the deprotonation of -OH in oxyhydroxides is accompanied by the abstraction of one electron from oxygen non-bonding state in a decoupled (or non-concerted) way, to generate a negatively charged oxygen ligand with more radical character ($\text{O}(-)$).⁵⁵⁻⁵⁶ The generation of the negatively charged species ($\text{*O}(-)$) would leave unpaired spin electrons on oxygens, while O^{2-} have all paired electrons. In the path for producing triplet oxygen, the step to create more unpaired spin electrons in ligand oxygens is a prerequisite for the start of spin polarization of oxygen radicals. Fig. 4b and 4c present the spin polarization mechanisms with and without the generation of $\text{O}(-)$ under AEM pathway. With abundant active oxygen ligands induced in 1st step, high density of spin electrons would have already been created at the ligand oxygen at 1st electron transfer step. However, with limited active oxygen ligand after 1st step, the ligand oxygens with great radical character could appear till the formation of the $\text{Co}^{\text{III}}\text{-OO}(-)$ intermediate, while the oxygens in $\text{Co}^{\text{IV}}\text{-O}$ and $\text{Co}^{\text{IV}}\text{-OO}(2-)$ intermediates have all paired electrons. Thus, with $\text{O}(-)$ in 1st step, the spin polarization has been facilitated before the O-O coupling, while without $\text{O}(-)$ after 1st step the spin polarization is hold until the creation of $\text{Co}^{\text{III}}\text{-OO}(-)$ intermediate. The early spin polarization on ligand oxygen will facilitate the subsequent O-O coupling with parallel spin alignment. The DFT was also carried out to study the free energy diagram along with the pathways with and without the $\text{O}(-)$ (Fig. 4f, left panel). In the modelling of the negatively charged species, all intermediates were added one negative charge and the surface layer of the system was fully relaxed to obtain optimized structure. The spin density of the *O with and without adding negative charge are examined, in which the $\text{*O}(-)$ shows higher spin density in non-bonding O p_{π} state (see detailed discussion in Supplementary Note 4 and Methods part). That demonstrates that $\text{O}(-)$ have higher density of unpaired O p electrons and with more radical character. With the involvement of the $\text{O}(-)$, the O-O coupling (rate-determining) is greatly facilitated and the overpotential is reduced by 360 mV as compared to that without the involvement of the $\text{O}(-)$.

For the OER steps with LOM, the spin polarization mechanisms are presented in the Fig. 4d and 4e. The critical step for the triplet oxygen production under LOM would be the formation of $\text{Co}^{\text{III}}\text{-OO}(-)$ intermediate, for which two oxygen radicals with parallel spin alignment are necessary (Supplementary Table 4). As the $\text{O}(-)$ is induced in the first deprotonation step, the spin polarization of oxygen radical under LOM also can start at earlier OER step. Moreover, two oxygen radicals can be induced in the 1st and 2nd electron transfer, in which one is from the ligand oxygen and another is from lattice oxygens. The two oxygen radicals can obtain parallel spin alignment under spin

pinning before the formation of $\text{Co}^{\text{III}}\text{-OO}(-)$ intermediate. The two oxygen radicals next to each other with parallel spins allow spin exchange of these two oxygen radicals and two oxygens close to each other, which finally leads to the formation of $\text{Co}^{\text{III}}\text{-OO}(-)$ intermediate. Without the $\text{O}(-)$ after 1st deprotonation step, there is additional barrier as the spins of two oxygen need to be aligned first before the formation of $\text{Co}^{\text{III}}\text{-OO}(-)$ intermediate, which leads to more overpotential for producing triplet oxygen. The DFT study (Fig. 4f, right panel) also reveals that the generation of Co-OO from Co-O is more preferable under LOM when $\text{O}(-)$ could be created in the 1st step. It is noted that the calculated LOM step ($\text{Co-O} \rightarrow \text{Co-OO}$) is downhill in free energy, which may indicate that this step is not the potential-limiting step (PLS) for OER. However, the activation barrier of this step could be very high during the O-O coupling, which makes this step still rate-limiting.⁵⁹ Considering the Brønsted–Evans–Polanyi (BEP) relation, the energy of the formation of the surface intermediates involved in the OER scales linearly with the logarithm of the activation energy.⁶⁰ It is thus still believed that the kinetic barrier is lowered when $\text{O}(-)$ is created in the 1st step.

Overall, in this study, the O-O coupling during OER is rate determining (energetically or kinetically), which could be facilitated by the spin polarization of $\text{O}(-)$ under spin pinning effect. As the generation of $\text{O}(-)$ is pH-dependent, the magnetization effect on OER activity is also pH-dependent. Similarly, as the spin pinning intrinsically exists, the pH-dependence is also found in the intrinsic activity of $\text{Co}_{2.75}\text{Fe}_{0.25}\text{O}_4/\text{Co}(\text{Fe})\text{O}_x\text{H}_y$. It should be also noted that such pH dependent OER activity could be also attributed to other non-concerted electron/transfer processes such as refilling the surface oxygen vacancy with OH^- .

Conclusion

We have designed a controllable surface reconstruction on ferromagnetic $\text{Co}_{3-x}\text{Fe}_x\text{O}_4$ spinels by low-level sulfurization. After reconstruction under alkaline OER, the pre-catalysts $\text{Co}_{3-x}\text{Fe}_x\text{O}_4$ (s) reached a stable $\text{Co}_{3-x}\text{Fe}_x\text{O}_4/\text{Co}(\text{Fe})\text{O}_x\text{H}_y$ configuration, where the oxyhydroxides layer is at limited depth of ~ 4 nm. Credited to the stable $\text{Co}_{3-x}\text{Fe}_x\text{O}_4/\text{Co}(\text{Fe})\text{O}_x\text{H}_y$ configuration with limited oxyhydroxides layer, the spin pinning effect has been introduced in oxyhydroxides, leading to higher intrinsic activity of reconstructed $\text{Co}(\text{Fe})\text{O}_x\text{H}_y$ than directly prepared $\text{Co}(\text{Fe})$ oxyhydroxides by ~ 1 order of magnitude. With the spin pinning effect, simple magnetization can further enhance the OER performance of $\text{Co}_{3-x}\text{Fe}_x\text{O}_4/\text{Co}(\text{Fe})\text{O}_x\text{H}_y$ ($x \neq 0$) as the pinned spins in $\text{Co}(\text{Fe})\text{O}_x\text{H}_y$ layer become more aligned along with the long-range FM ordering of magnetic domains in $\text{Co}_{3-x}\text{Fe}_x\text{O}_4$ substrate. Moreover, it is also believed that the generated active oxygen ligands in reconstructed oxyhydroxide is critical for the spin polarization

of ligand oxygen during OER. When it is generated in the 1st deprotonation step in high pH media, the ligand oxygens have more unpaired p electrons in non-bonding state and with more radical character. Under spin pinning, the spin polarization of the oxygen radicals can be facilitated, which reduces the barrier for subsequent O-O coupling. Overall, our design takes the advantage of a controllable surface reconstruction on ferromagnetic oxides to realize the spinning pinning effect in Co oxyhydroxides. The usage of spin pinning effect is an effective way to stabilize extended ferromagnetic orderings in active compositions, like Co oxyhydroxides in our case, and is a promising way of engineering QSEI in non-ferromagnetic catalysts to improve catalysis. It is of great significance because in the family of excellent OER catalysts, many of them are hydroxides, oxyhydroxides, layer double hydroxides (LDHs) and even some active perovskites that exhibit no long-range ferromagnetism. The spin pinning effect provides them with a great potential for boosting spin-dependent kinetics to further enhance OER performance. Besides, the strategy toward controllable surface reconstruction of oxides would also contribute to designing high-performing pre-catalysts without compromising the bulk stability of reconstructed catalysts.

Reference

1. Suntivich, J., et al., A perovskite oxide optimized for oxygen evolution catalysis from molecular orbital principles. *Science* **334**, 1383-1385 (2011).
2. Koper, M. T. M., Thermodynamic theory of multi-electron transfer reactions: Implications for electrocatalysis. *Journal of Electroanalytical Chemistry* **660**, 254-260 (2011).
3. Chao, W., et al., Cations in Octahedral Sites: A Descriptor for Oxygen Electrocatalysis on Transition-Metal Spinels. *Advanced Materials* **29**, 1606800 (2017).
4. Fabbri, E., et al., Dynamic surface self-reconstruction is the key of highly active perovskite nano-electrocatalysts for water splitting. *Nat Mater* **16**, 925-931 (2017).
5. Risch, M., et al., Structural Changes of Cobalt-Based Perovskites upon Water Oxidation Investigated by EXAFS. *J. Phys. Chem. C* **117**, 8628-8635 (2013).
6. Görlin, M., et al., Tracking Catalyst Redox States and Reaction Dynamics in Ni-Fe Oxyhydroxide Oxygen Evolution Reaction Electrocatalysts: The Role of Catalyst Support and Electrolyte pH. *J. Am. Chem. Soc.* **139**, 2070-2082 (2017).
7. Smith, R. D. L., et al., Spectroscopic identification of active sites for the oxygen evolution reaction on iron-cobalt oxides. *Nat. Commun.* **8**, 2022 (2017).
8. Bergmann, A., et al., Reversible amorphization and the catalytically active state of crystalline Co₃O₄ during oxygen evolution. *Nat. Commun.* **6**, 8625 (2015).
9. Wu, T., et al., Iron-facilitated dynamic active-site generation on spinel CoAl₂O₄ with self-termination of surface reconstruction for water oxidation. *Nature Catalysis* **2**, 763-772 (2019).
10. Gracia, J., Spin dependent interactions catalyse the oxygen electrochemistry. *Physical Chemistry Chemical Physics* **19**, 20451-20456 (2017).
11. Mtangi, W., et al., Control of Electrons' Spin Eliminates Hydrogen Peroxide Formation During Water Splitting. *Journal of the American Chemical Society* **139**, 2794-2798 (2017).
12. Gracia, J., Itinerant Spins and Bond Lengths in Oxide Electrocatalysts for Oxygen Evolution and Reduction Reactions. *The Journal of Physical Chemistry C* **123**, 9967-9972 (2019).

- 509 13. Torun, E.; Fang, C. M.; de Wijs, G. A.; de Groot, R. A., Role of Magnetism in Catalysis: RuO₂ (110) Surface. *The*
510 *Journal of Physical Chemistry C* **117**, 6353-6357 (2013).
- 511 14. Garcés-Pineda, F. A., et al., Direct magnetic enhancement of electrocatalytic water oxidation in alkaline media. *Nature*
512 *Energy* **4**, 519-525 (2019).
- 513 15. Gracia, J.; Sharpe, R.; Munarriz, J., Principles determining the activity of magnetic oxides for electron transfer reactions.
514 *Journal of Catalysis* **361**, 331-338 (2018).
- 515 16. Goodenough, J. B., Electronic and ionic transport properties and other physical aspects of perovskites. *Reports on*
516 *Progress in Physics* **67**, 1915-1993 (2004).
- 517 17. Burke, M. S., et al., Cobalt–Iron (Oxy)hydroxide Oxygen Evolution Electrocatalysts: The Role of Structure and
518 Composition on Activity, Stability, and Mechanism. *J. Am. Chem. Soc.* **137**, 3638-3648 (2015).
- 519 18. Khassin, A. A., et al., Physico-chemical study on the state of cobalt in a precipitated cobalt-aluminum oxide system.
520 *Physical Chemistry Chemical Physics* **4**, 4236-4243 (2002).
- 521 19. Kudielka, A., et al., Variability of composition and structural disorder of nanocrystalline CoOOH materials. *Journal of*
522 *Materials Chemistry C* **5**, 2899-2909 (2017).
- 523 20. Berkowitz, A. E., et al., Spin Pinning at Ferrite-Organic Interfaces. *Physical Review Letters* **34**, 594-597 (1975).
- 524 21. Ong, Q. K.; Wei, A.; Lin, X.-M., Exchange bias in Fe/Fe₃O₄ core-shell magnetic nanoparticles mediated by frozen
525 interfacial spins. *Physical Review B* **80**, 134418 (2009).
- 526 22. Sparks, M., Theory of Surface-Spin Pinning in Ferromagnetic Resonance. *Physical Review Letters* **22**, 1111-1115
527 (1969).
- 528 23. Duan, Y., et al., Mastering Surface Reconstruction of Metastable Spinel Oxides for Better Water Oxidation. *Advanced*
529 *Materials* **31**, 1807898 (2019).
- 530 24. Xu, Z. J., Transition metal oxides for water oxidation: All about oxyhydroxides? *Science China Materials*, (2019).
- 531 25. Grimaud, A., et al., Activating lattice oxygen redox reactions in metal oxides to catalyse oxygen evolution. *Nat. Chem.*
532 **9**, 457-465 (2017).
- 533 26. May, K. J., et al., Influence of Oxygen Evolution during Water Oxidation on the Surface of Perovskite Oxide Catalysts.
534 *J. Phys. Chem. Lett.* **3**, 3264-3270 (2012).
- 535 27. Song, J., Are Metal Chalcogenides, Nitrides, and Phosphides Oxygen Evolution Catalysts or Bifunctional Catalysts?
536 *ACS Energy Letters* **2**, 1937-1938 (2017).
- 537 28. Zhai, S.-Y.; Li, L.-L.; Wang, M.-G., A facile synthesis about amorphous CoS₂ combined with first principle analysis
538 for supercapacitor materials. *Ionics* **23**, 1819-1830 (2017).
- 539 29. Pauling, L., Covalent chemical bonding of transition metals in pyrite, cobaltite, skutterudite, millerite and related
540 minerals. *The Canadian Mineralogist* **16**, 447-452 (1978).
- 541 30. Mabayoje, O.; Shoola, A.; Wygant, B. R.; Mullins, C. B., The Role of Anions in Metal Chalcogenide Oxygen Evolution
542 Catalysis: Electrodeposited Thin Films of Nickel Sulfide as “Pre-catalysts”. *ACS Energy Letters* **1**, 195-201 (2016).
- 543 31. Bøckman, O.; Østvold, T.; Voyiatzis, G. A.; Papatheodorou, G. N., Raman spectroscopy of cemented cobalt on zinc
544 substrates. *Hydrometallurgy* **55**, 93-105 (2000).
- 545 32. Shieh, S. R.; Duffy, T. S., Raman spectroscopy of Co(OH)₂ at high pressures: Implications for amorphization and
546 hydrogen repulsion. *Physical Review B* **66**, 134301 (2002).
- 547 33. Yang, J.; Liu, H.; Martens, W. N.; Frost, R. L., Synthesis and Characterization of Cobalt Hydroxide, Cobalt
548 Oxyhydroxide, and Cobalt Oxide Nanodiscs. *The Journal of Physical Chemistry C* **114**, 111-119 (2010).
- 549 34. Wei, C., et al., Approaches for measuring the surface areas of metal oxide electrocatalysts for determining their intrinsic
550 electrocatalytic activity. *Chemical Society Reviews* **48**, 2518-2534 (2019).
- 551 35. Sun, S.; Li, H.; Xu, Z. J., Impact of Surface Area in Evaluation of Catalyst Activity. *Joule* **2**, 1024-1027 (2018).
- 552 36. Hadjiev, V. G.; Iliev, M. N.; Vergilov, I. V., The Raman spectra of Co₃O₄. *Journal of Physics C: Solid State Physics* **21**,

553 L199-L201 (1988).
 554 37. Gu, H.; Xu, K.; Xu, C.; Xu, B., Biofunctional Magnetic Nanoparticles for Protein Separation and Pathogen Detection.
 555 *ChemInform* **37**, (2006).
 556 38. López-Ortega, A., et al., Applications of exchange coupled bi-magnetic hard/soft and soft/hard magnetic core/shell
 557 nanoparticles. *Physics Reports* **553**, 1-32 (2015).
 558 39. Berkowitz, A. E.; Takano, K., Exchange anisotropy — a review. *Journal of Magnetism and Magnetic Materials* **200**,
 559 552-570 (1999).
 560 40. Nogués, J.; Schuller, I. K., Exchange bias. *Journal of Magnetism and Magnetic Materials* **192**, 203-232 (1999).
 561 41. Haneda, K.; Morrish, A., Magnetic structure at γ -Fe₂O₃-organic interfaces. *IEEE Transactions on Magnetics* **16**, 50-52
 562 (1980).
 563 42. Morr, A. H.; Haneda, K., Magnetic structure of small NiFe₂O₄ particles. *Journal of Applied Physics* **52**, 2496-2498
 564 (1981).
 565 43. Dutta, P.; Seehra, M. S.; Thota, S.; Kumar, J., A comparative study of the magnetic properties of bulk and
 566 nanocrystalline Co₃O₄. *Journal of Physics: Condensed Matter* **20**, 015218 (2007).
 567 44. Zhou, B. H.; Rinehart, J. D., A Size Threshold for Enhanced Magnetoresistance in Colloidally Prepared CoFe₂O₄
 568 Nanoparticle Solids. *ACS Central Science* **4**, 1222-1227 (2018).
 569 45. Risch, M., et al., La_{0.8}Sr_{0.2}MnO₃- δ Decorated with Ba_{0.5}Sr_{0.5}Co_{0.8}Fe_{0.2}O₃- δ : A Bifunctional Surface for Oxygen
 570 Electrocatalysis with Enhanced Stability and Activity. *Journal of the American Chemical Society* **136**, 5229-5232 (2014).
 571 46. Hong, W. T., et al., Toward the rational design of non-precious transition metal oxides for oxygen electrocatalysis.
 572 *Energy & Environmental Science* **8**, 1404-1427 (2015).
 573 47. Kanan, M. W.; Nocera, D. G., In Situ Formation of an Oxygen-Evolving Catalyst in Neutral Water Containing
 574 Phosphate and Co²⁺. *Science* **321**, 1072-1075 (2008).
 575 48. Roy, C., et al., Impact of nanoparticle size and lattice oxygen on water oxidation on NiFeOxHy. *Nature Catalysis* **1**,
 576 820-829 (2018).
 577 49. Trotochaud, L.; Young, S. L.; Ranney, J. K.; Boettcher, S. W., Nickel-iron oxyhydroxide oxygen-evolution
 578 electrocatalysts: the role of intentional and incidental iron incorporation. *Journal of the American Chemical Society* **136**,
 579 6744-6753 (2014).
 580 50. Chen, Y., et al., Exceptionally active iridium evolved from a pseudo-cubic perovskite for oxygen evolution in acid.
 581 *Nature Communications* **10**, 572 (2019).
 582 51. Liu, Y., et al., Ultrathin Co₃S₄ Nanosheets that Synergistically Engineer Spin States and Exposed Polyhedra that
 583 Promote Water Oxidation under Neutral Conditions. *Angewandte Chemie International Edition* **54**, 11231-11235 (2015).
 584 52. Ojha, V. H.; Kant, K. M., Temperature dependent magnetic properties of superparamagnetic CoFe₂O₄ nanoparticles.
 585 *Physica B: Condensed Matter* **567**, 87-94 (2019).
 586 53. Wandt, J.; Freiberg, A. T. S.; Ogrodnik, A.; Gasteiger, H. A., Singlet oxygen evolution from layered transition metal
 587 oxide cathode materials and its implications for lithium-ion batteries. *Materials Today* **21**, 825-833 (2018).
 588 54. Sharpe, R., et al., Orbital Physics of Perovskites for the Oxygen Evolution Reaction. *Topics in Catalysis* **61**, 267-275
 589 (2018).
 590 55. Yang, C.; Fontaine, O.; Tarascon, J. M.; Grimaud, A., Chemical Recognition of Active Oxygen Species on the Surface
 591 of Oxygen Evolution Reaction Electrocatalysts. *Angewandte Chemie International Edition* **56**, 8652-8656 (2017).
 592 56. Diaz-Morales, O.; Ferrus-Suspedra, D.; Koper, M. T. M., The importance of nickel oxyhydroxide deprotonation on its
 593 activity towards electrochemical water oxidation. *Chemical Science* **7**, 2639-2645 (2016).
 594 57. Huang, Z.-F., et al., Chemical and structural origin of lattice oxygen oxidation in Co-Zn oxyhydroxide oxygen
 595 evolution electrocatalysts. *Nature Energy* **4**, 329-338 (2019).
 596 58. Koper, M. T. M., Theory of multiple proton-electron transfer reactions and its implications for electrocatalysis.

Chemical Science **4**, 2710-2723 (2013).

59. Soriano-López, J.; Schmitt, W.; García-Melchor, M., Computational modelling of water oxidation catalysts. *Current Opinion in Electrochemistry* **7**, 22-30 (2018).

60. Nørskov, J. K., et al., The nature of the active site in heterogeneous metal catalysis. *Chem. Soc. Rev.* **37**, 2163-2171 (2008).

Acknowledgements

T. W. and X.R. contribute equally to this work. Authors thank the support from the National Nature Science Foundation of China (Grant No. 11274370, and 51471185) and the National Natural Key R&D Program of China (Grant No. 2016YFA0202301 and 2018FYA0305800). Authors in Singapore thank the support from the Singapore Ministry of Education Tier 2 Grants (MOE2017-T2-1-009 and MOE2018-T2-2-027). Authors appreciate the Facility for Analysis, Characterisation, Testing and Simulation (FACTS) in Nanyang Technological University for materials characterizations. This work was partially supported by the National Research Foundation (NRF), Prime Minister's Office, Singapore under its Campus for Research Excellence and Technological Enterprise (CREATE) programme through the SHARE NEW Phase II project and the eCO2EP project operated by the Cambridge Centre for Advanced Research and Education in Singapore (CARES) and the Berkeley Educational Alliance for Research in Singapore (CARES). **This manuscript was submitted to Nature Energy (NENERGY-19112344) on 04-Dec-2019.**

Author contributions

Z.X., T.W., and S.S. conceived the original concept. Z.X., T.W., X.R., and H.Y. designed the experiments. T.W. prepared the materials and performed most characterizations. H.Y., X.R and T.W carried out magnetic property measurements. G.X. and T.W. performed the Raman spectroscopy measurement. Y.S. contributed the DFT calculations and analysis. J.G. contributed the explanation of QSEI theory. T.W. plotted all figures and wrote the manuscript with the input from all authors. All authors engaged in the analysis of experimental results and manuscript edition.

Competing interests

The authors declare no competing financial interests.

Supplementary materials

Controlled surface reconstruction on ferromagnetic oxides: spin pinning effect to the oxyhydroxide layer and its enhanced oxygen evolution activity

Tianze Wu^{1,2,3,Δ}, Xiao Ren^{1,2,Δ}, Yuanmiao Sun², Shengnan Sun², Guoyu Xian¹, Günther G. Scherer^{4,5}, Adrian C. Fisher⁶, Daniel Mandler^{7,8}, Joel W. Ager^{9,10}, Alexis Grimaud^{11,12}, Junling Wang², Chengmin Shen¹, Haitao Yang^{1}, Jose Gracia¹³, Hong-Jun Gao¹, Zhichuan J. Xu^{2,3,14*}*

¹Beijing National Laboratory for Condensed Matter Physics and Institute of Physics, Chinese Academy of Science, Beijing 100190, China;

²School of Materials Science and Engineering, Nanyang Technological University, 50 Nanyang Avenue, 639798, Singapore;

³Solar Fuels Laboratory and Energy Research Institute, Nanyang Technological University, 50 Nanyang Avenue, 639798, Singapore;

⁴Department for Management of Science and Technology Development, Ton Duc Thang University, Ho Chi Minh City, Vietnam;

⁵Faculty of Applied Sciences, Ton Duc Thang University, Ho Chi Minh City, Vietnam;

⁶Department of Chemical Engineering, University of Cambridge, Cambridge CB2 3RA, UK;

⁷Institute of Chemistry, The Hebrew University of Jerusalem, Jerusalem 9190401, Israel;

⁸Singapore-HUJ Alliance for Research and Enterprise (SHARE), Nanomaterials for Energy and Energy-Water Nexus (NEW), Campus for Research Excellence and Technological Enterprise (CREATE), 138602, Singapore;

⁹Department of Materials Science and Engineering, University of California at Berkeley, Berkeley, California 94720, USA;

¹⁰Berkeley Educational Alliance for Research in Singapore (BEARS), Ltd., 1 CREATE Way, 138602, Singapore

¹¹Chimie du Solide et de l'Energie, UMR 8260, Collège de France, 75231 Paris Cedex 05, France;

¹²Réseau sur le Stockage Electrochimique de l'Energie (RS2E), CNRS FR 3459, 33 rue Saint Leu, 80039, Amiens Cedex, France;

¹³MagnetoCat SL, General Polavieja 9 3I, 03012 Alicante, Spain;

¹⁴Energy Research Institute @ Nanyang Technological University, 50 Nanyang Avenue, Singapore 639798, Singapore.

^ΔThese authors contribute equally to this work.

*Corresponding authors: xuzc@ntu.edu.sg (Z. Xu), htyang@iphy.ac.cn (H. Yang)

Methods

Co_{3-x}Fe_xO₄ oxides synthesis. Co_{3-x}Fe_xO₄ (x=0, 0.25, 1, 2) spinel oxides were synthesized by a sol-gel method as described elsewhere.¹ Cobalt acetate (Co(OAc)₂·4H₂O) and Iron(III) nitrate nonahydrate (Fe(NO₃)₃ · 9H₂O) were mixed in specific molar ratio according to the elemental ratio in products, then dissolving in the diluted nitric acid. Citric acid and urea were added into the solution, which was followed by stirring and heating up at 80-100 °C to form a viscous gel. The gel was dried and decomposed in air box at 170 °C for 12 hours. Finally, the calcination was carried at 400~600 °C for 6 hours to obtain Co_{3-x}Fe_xO₄ (x=0, 0.25, 1, 2) spinel oxides.

Sulfurization of Co_{3-x}Fe_xO₄ oxides. The as-prepared Co_{3-x}Fe_xO₄ and sulfur powder were mixed in a mortar with a mass ratio of 10:1. The mixtures were sealed in a glassy tube under Ar atmosphere, which was followed by heating under 300 °C for 6 hours. The sulfurization degree was decided by Inductively Coupled Plasma Optical Emission Spectrometry (ICP-OES). The results are summarized in Supplementary Table 1.

Materials characterization. The X-ray diffraction (XRD) of Co_{3-x}Fe_xO₄ were carried on Bruker D8 diffractometer at a scanning rate of 2° min⁻¹, under Cu-K_α radiation (λ = 1.5418 Å). The BET (Brunauer-Emmett-Teller) measurement was conducted on ASAP Tristar II 3020 from single-point BET analysis. All samples were performed after 12 h outgassing at 170 °C. The BET surface area of Co_{3-x}Fe_xO₄ oxides and their synthesis parameters are summarized in Supplementary Table 2. The high-resolution transmission electron microscopy (HRTEM) was carried JEOL JEM- 2100 plus microscope at 200KV. The Fourier transform infrared spectroscopy–Raman spectroscopy was carried with a confocal Raman microscope (Labram HR EV0), equipped with a diode laser emitting at 532 nm at a nominal power of 12 mW. Laser power was limited at nominal 10% to avoid damaging samples. Spectra were recorded with the accumulation time of 60 s. For obtaining the Raman spectra of cycled catalysts, the catalysts were coated on carbon papers by drop casting for CV cycling in 1M KOH (10 cycles), then dried under N₂ gas before measurements.

Electrochemical characterization. The working electrodes were fabricated by drop casting on glassy carbon electrodes. The powder samples were mixed with acetylene black (AB) at a mass ration of 5:1, then were dispersed in isopropanol/water (v/v=1:4) solvent followed by the addition of Na⁺-exchanged Nafion as the binder. The mixtures were ultrasonicated for 20 min to reach homogeneous ink. Before drop casting, the glassy carbon electrodes were polished to a mirror finish with α-Al₂O₃ (50 nm) and washed by IPA and

water to completely clean up. Finally, the as-prepared ink (10 μ l) was dropped onto glassy carbon electrodes (0.196 cm^2) to reach a loading mass of 255 $\mu\text{g}_{\text{ox}} \text{cm}^{-2}$ and the electrodes were dried overnight at room temperature.

The electrochemical tests were conducted in a three-electrode system using $\text{Co}_{3-x}\text{Fe}_x\text{O}_4$ electrode as working electrode, platinum plate ($1 \times 2 \text{ cm}^2$) as the counter electrode, Hg/HgO (1M KOH, aqueous, MMO) as the reference. The cyclic voltammetry (CV) and linear sweep voltammetry (LSV) are performed at a scan rate of 10 mV s^{-1} in O_2 -saturated 1.0 M KOH by using Bio-logic SP 150 potentiostat. All potentials measured are converted to RHE scale and under iR correction. The RHE reference calibration experiment was conducted by performing cyclic voltammetry (CV) measurements in the voltage range of hydrogen electrocatalysis (HER/HOR) in H_2 -saturated 1M KOH using Pt as the working electrode (Supplementary Fig. 28).² The E_{offset} was obtained as the conversion factor: $E (\text{vs. RHE}) = E (\text{vs. Hg/HgO}) - E_{\text{offset}} = E (\text{vs. Hg/HgO}) + 0.932 (\text{V})$. The TOF was obtained according to the equation:

$$\text{TOF} = \frac{j \times A}{4Fn}$$

Where j is the current density ($\text{A cm}_{\text{disk}}^{-2}$) delivered at an overpotential of 350 mV; A is the disk area of glassy carbon electrode (0.196 cm^2), F is the Faraday constant (96485 C/mol); n is the number of active sites (mole). n is estimated by either assuming all active metal atoms in the active species are effective (denoted as “bulk”) or calculating only the active metal atoms on the surface (denoted as “surface”). The TOF_{bulk} and $\text{TOF}_{\text{surface}}$ of some catalysts present the low and upper limit of the estimated TOF for fair comparison. The n_{surface} is obtained by an average integral area of the $\text{Co}^{2+}/\text{Co}^{3+}$ anodic and cathodic peaks (Supplementary Fig. 29). The n_{bulk} of the reconstructed $\text{Co}(\text{Fe})\text{O}_x\text{H}_y$ is estimated by assuming all Co in the sulfurized $\text{Co}_{2.75}\text{Fe}_{0.25}\text{O}_4$ surface have reconstructed into active oxyhydroxides, where the sulfurized degree of 2.06% is given by the ICP measurement. The n_{surface} is estimated by the integral area of the $\text{Co}^{2+}/\text{Co}^{3+}$ redox peaks (A_{redox}) to obtain the population of Co that are electrochemically active on the surface (Supplementary Fig. 29). The j and A_{redox} of $\text{Co}(\text{Fe})\text{O}_x\text{H}_y$ are obtained from the 2nd cycle in CVs, followed by the correction of subtracting the background signals from $\text{Co}_{2.75}\text{Fe}_{0.25}\text{O}_4$ substrate. The n_{bulk} of $\text{Co}_{0.86}\text{Fe}_{0.14}(\text{OOH})$ is reported to be estimated according to the measurement of the catalyst mass and composition by *in-situ* QCM and *ex-situ* XPS.³ The n_{surface} is calculated by $n_{\text{bulk}}/x\%$, where $x\%$ is the fraction of Co in deposited $\text{Co}_{0.86}\text{Fe}_{0.14}(\text{OOH})$ that is electrochemically active ($x\%=27\%$, 2nd cycle).³ The n_{bulk} of BSCF film is reported to be calculated according to the unit cell volume, film thickness, and electrode area. The n_{surface} is reported to be determined by calculating the number of atoms on an assumed (100) surface according to the refined lattice parameters and the surface area of oxides that is decided by Brunauer-Emmett-Teller (BET) measurement. The n_{surface} of “Co-Pi” is reported to be obtained by the surface density of “Co-Pi” from EXAFS characterization.⁴ The n_{surface} of $\text{Ni}_{0.75}\text{Fe}_{0.25}\text{O}_x\text{H}_y$ on both Au and GC electrode are reported to be estimated by the integral of the Ni^{2+} to $\text{Ni}^{3+/4+}$ redox couple in CVs.⁵ The reported n_{bulk} for $\text{Ni}_{0.75}\text{Fe}_{0.25}\text{O}_x\text{H}_y$ NPs and electrodeposited $\text{Ni}_{0.75}\text{Fe}_{0.25}\text{O}_x\text{H}_y$ are very close to their n_{surface} .⁵⁻⁶ The n_{surface} of IrO_2 is reported to be estimated according to refined lattice parameters with consideration of a (110) surface, and the oxide surface area that is determined by BET measurement.⁷ The n_{bulk} of BSCF, “Co-Pi”, IrO_2 and Co_3S_4 are estimated by all

active metal atoms in the catalysts loaded on the electrodes.

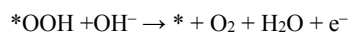
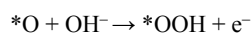
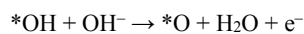
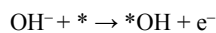
SQUID Measurement.

DC magnetization measurements were performed on a Superconducting Quantum Design (SQUID) magnetometer (MPMS-XL). The $\text{Co}_x\text{Fe}_{3-x}\text{O}_4$ powders were accurately weighted before measurements. The SQUID measurements of the magnetization of $\text{Co}_x\text{Fe}_{3-x}\text{O}_4$ powders as a function of magnetic field were carried out at 300 K in fields between -5 T and +5 T. For measuring the exchange bias of $\text{CoFe}_2\text{O}_4/\text{Co}(\text{Fe})\text{O}_x\text{H}_y$, the $\text{CoFe}_2\text{O}_4(\text{s})$ samples were coated on carbon film by drop casting and following the procedure same as that in electrochemical measurements. After cycling, the samples were dried under N_2 ambience before SQUID measurements. The SQUID measurement was then carried under field-cooled (FC, 5T) mode and zero-field-cooled (ZFC) mode and at a temperature of 2 K.

Computational Method.

All the density functional theory (DFT) calculations were performed by Vienna Ab-initio Simulation Package⁸⁻⁹ (VASP), employing the Projected Augmented Wave¹⁰ (PAW) method. The revised Perdew-Burke-Ernzerhof (RPBE) functional was used to describe the exchange and correlation effects.¹¹⁻¹³ For all the geometry optimizations, the cutoff energy was set to be 450 eV. A $4 \times 2 \times 1$ Monkhorst-Pack grids¹⁴ was used to carry out the surface calculations on the layered oxyhydroxides. At least 20 Å vacuum layer was applied in z-direction of the slab models, preventing the vertical interactions between slabs.

In alkaline conditions, OER could occur in the following four elementary steps:



where * denotes the active sites on the catalyst surface. Based on the above mechanism, the free energy of three intermediate states, *OH, *O, and *OOH, are important to determine the OER activity of a given material. The computational hydrogen electrode (CHE) model¹⁵ was used to calculate the free energies of OER. The free energy of the adsorbed species is defined as

$$\Delta G_{ads} = \Delta E_{ads} + \Delta E_{ZPE} - T\Delta S_{ads}$$

where ΔE_{ads} is the electronic adsorption energy, ΔE_{ZPE} is the zero point energy difference between adsorbed and gaseous species, and $T\Delta S_{ads}$ is the corresponding entropy difference between these two states. The electronic binding energy is referenced as $\frac{1}{2} \text{H}_2$ for each H atom, and $(\text{H}_2\text{O} - \text{H}_2)$ for each O atom, plus the energy of the clean slab. The corrections of zero point energy and entropy of the OER intermediates can be found in Supplementary Table 3. For the modelling of negatively charged oxygen, the charge of oxygen was added

with NELECT parameters in VASP. During the calculations, the surface layer of the system was allowed to fully relax while the bottom layers were kept fixed. The energy of the charged system was obtained after structural optimization. The slab models for calculating the free energy along with reaction coordinates are shown in Supplementary Fig. 26.

Supplementary Note 1. The reconstruction can be controlled by the sulfurization degree of pristine oxides. The $\text{Co}_{2.75}\text{Fe}_{0.25}\text{O}_4$ was mixed with sulfur powder at mass ratios of 5:0.5, 5:1, and 5:3, followed by heat treatment for sulfurization. The sulfurization degree is estimated according to the ICP-OES measurement of sulfurized samples ($\text{Co}_{2.75}\text{Fe}_{0.25}\text{O}_4$ (s)) (Supplementary Table 1). The CVs (1st and 2nd cycle) of $\text{Co}_{2.75}\text{Fe}_{0.25}\text{O}_4$ (s) are given in Supplementary Fig. 3a-3f. The irreversible pseudocapacitive charge in the 1st cycle indicates the irreversible oxidation during the surface reconstruction of $\text{Co}_{2.75}\text{Fe}_{0.25}\text{O}_4$ (s). Such signal for reconstruction become more notable along with the increase of sulfurization degree. Accordingly, the reconstructed $\text{Co}_{2.75}\text{Fe}_{0.25}\text{O}_4$ / $\text{Co}(\text{Fe})\text{O}_x\text{H}_y$ can deliver higher current density with higher-degree reconstruction. The reconstructed $\text{Co}_{2.75}\text{Fe}_{0.25}\text{O}_4$ (s) samples were observed under HRTEM (Supplementary Fig. 4a-4c). For all samples, an oxyhydroxide layer that is resulted by reconstruction can be found on the $\text{Co}_{2.75}\text{Fe}_{0.25}\text{O}_4$ substrate. In Supplementary Fig. 5, the thickness of the oxyhydroxide layer has been estimated and correlated linearly to the sulfurization degree of $\text{Co}_{2.75}\text{Fe}_{0.25}\text{O}_4$ (s).

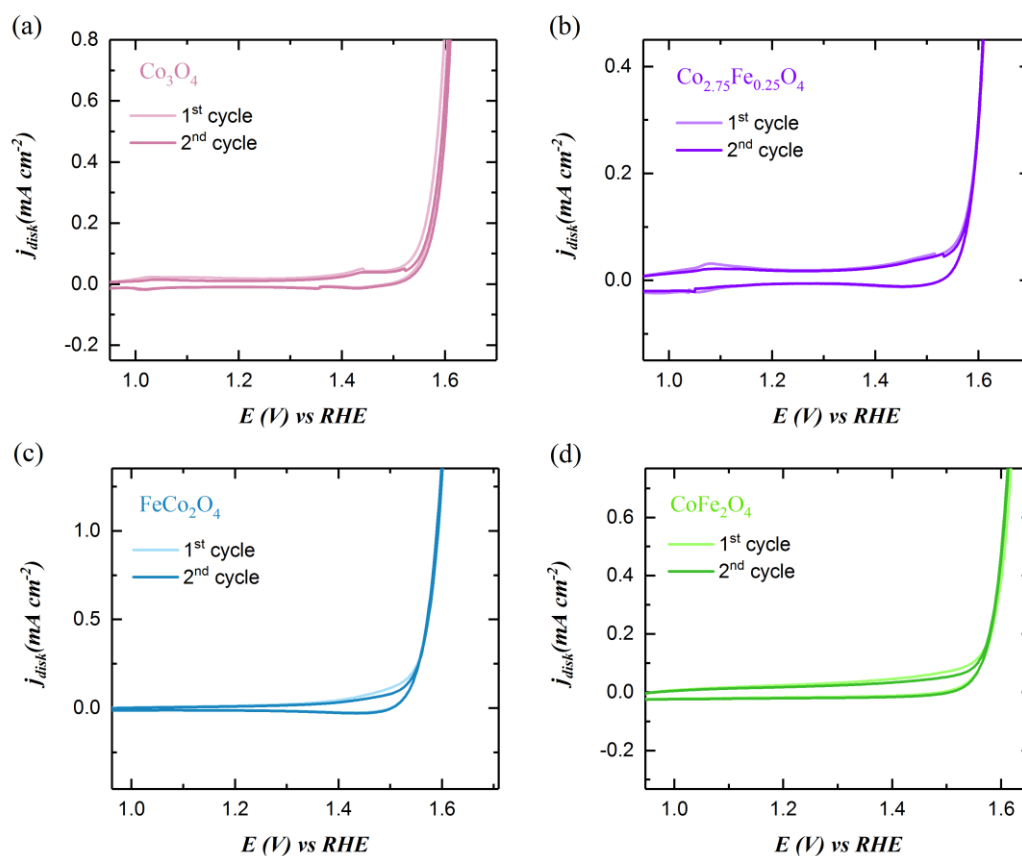
Supplementary Note 2. As the activity of $\text{Co}(\text{Fe})$ oxyhydroxide is also sensitive to the Co/Fe ratio, we synthesized the $\text{Co}_{0.9}\text{Fe}_{0.1}\text{OOH}$ and referenced the benchmark $\text{Co}_{0.86}\text{Fe}_{0.14}\text{OOH}^3$ for the comparison with $\text{Co}_{2.75}\text{Fe}_{0.25}\text{O}_4/\text{Co}(\text{Fe})\text{OOH}$ (assuming that the Co/Fe ratio will not change remarkably after the surface reconstruction). The $\text{Co}_{0.9}\text{Fe}_{0.1}\text{OOH}$ was synthesized according to a reported hydrothermal method.¹⁶ The HRTEM image and the FFT patterns of $\text{Co}_{0.9}\text{Fe}_{0.1}\text{OOH}$ are shown in Supplementary Fig. 9a and 9b. The steady CV of $\text{Co}_{0.9}\text{Fe}_{0.1}\text{OOH}$ at a scan rate of 10 mV s^{-1} in 1 M KOH is shown in Supplementary Fig. 9c. The surface area of $\text{Co}_{0.9}\text{Fe}_{0.1}\text{OOH}$ is indicated by BET measurement (Supplementary Fig. 8e).

Supplementary Note 3. The measurement of $\text{CoFe}_2\text{O}_4/\text{Co}(\text{Fe})\text{O}_x\text{H}_y$ was also performed in a two-electrode cell before and after magnetization. The OER performance of $\text{CoFe}_2\text{O}_4/\text{Co}(\text{Fe})\text{O}_x\text{H}_y$ exhibits notable enhancement after magnetization (Supplementary Fig. 30a). This result excludes the possible influence of magnetization on the reference electrode. Moreover, magneto-hydrodynamic (MHD) effect under a magnetic field has been found to improve the mass transportation of ions near the electrode surface. The MHD effect originates from the Lorentz force that affects the direction of charged ions M^{x+} movement in electrolyte. The MHD effect decreases the thickness of the diffusion layer, which thus increases the limiting current in cathodic reactions such as metal electrodeposition. However,

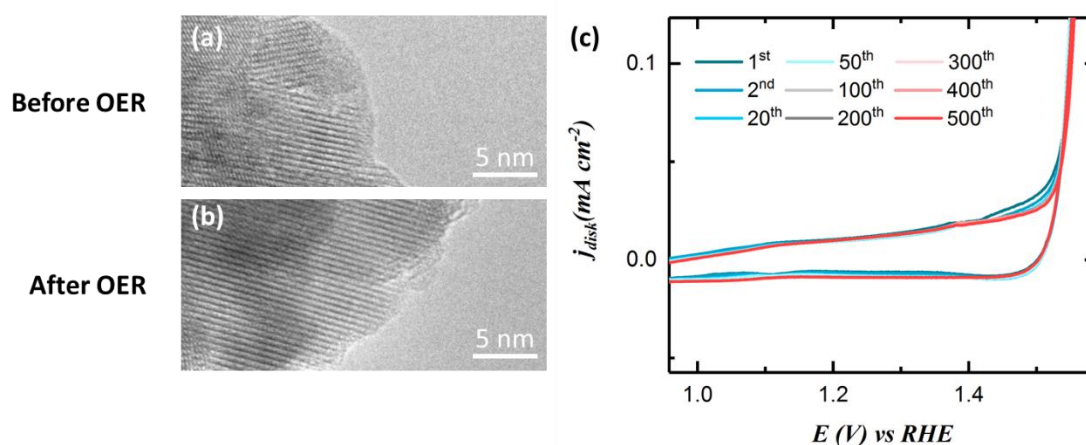
such an effect on ions may not be applicable to OER in aqueous solution. It has been well understood that OH^- in aqueous solution do not move physically, but by sequential proton hopping, known as Grotthuss mechanisms (Supplementary Fig. 30b)¹⁷. That means there is actually no physical movement of OH^- ions and thus the influence of Lorentz force on the OH^- or H_3O^+ is negligible. It can be excluded that the observed enhancement is from the MHD effect. In addition, it has been known that the MHD effect can promote the gas bubble release and thus improve the HER and OER kinetics. However, that was under the high overpotential and high current region, in which the gas bubble release significantly affects the reaction kinetics.¹⁸⁻¹⁹ It is not the case in the experiments presented in this work.

Supplementary Note 4. The ligand oxygen with unpaired p states localized in π non-bonding orbitals can be more appropriately described as oxygen radical.²⁰ The radical character of ligand oxygen is examined with and without negative charge. The orbital-specified DOS of oxygen in $^*\text{O}$ intermediate with and without negative charge are provided in Supplementary Fig. 25a and 25b. The O p states below Fermi level greatly split, because the electrons are localized in bonding state and non-bonding state. As seen, the $\sigma_{\text{Co-O}}$ bonding orbitals are localized in O $2p_z$ while the non-bonding (nb) orbitals are greatly localized in O p_x and p_y . When the O p_π (p_x and p_y) is in non-bonding state, the oxygen is better described as oxygen radical (Supplementary Fig. 25c). We also found a spin density of 0.828 on the oxygen radical, indicating unpaired p electron in ligand oxygen. Moreover, the magnetization (spin density) of Co and O are summarized in Supplementary Table 4. The magnetization of Co in all intermediates are below 4, which implies Co^{III} is more appropriate in the calculations. Overall, the DFT study indicate that Co(III)-oxyl radical should be more preferred than Co(IV)-oxo .

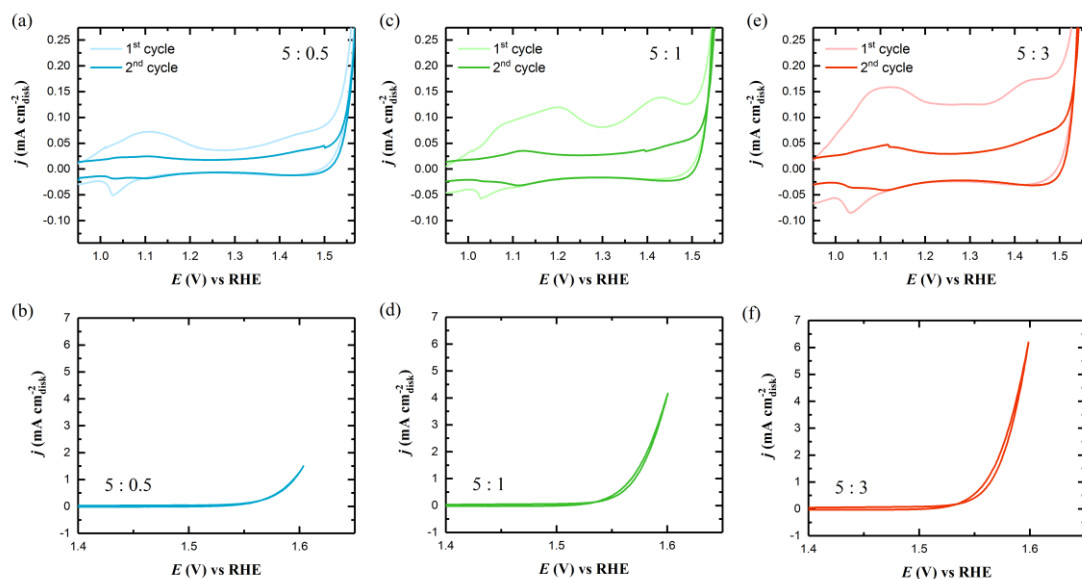
The negative charge was added to model the negatively charged species ($^*\text{O}(-)$) generated under high pH (higher than the pK_a of the proton attached to the CoO(OH) species).²¹ It should be noted that the charge was added to all intermediates and the reaction coordinate keeps one-electron-per-step process to avoid the influence of the energy shift by adding charge on any elementary step. In the orbital-specified DOS of ligand oxygen with and without charge (Supplementary Fig. 25a and 25b), It is found that the added negative charge greatly affects the localized O p_x and p_y orbitals (non-bonding state) of ligand oxygen. In the overall DOS of the ligand oxygen with and without charge (Supplementary Fig. 25d), the unpaired state ($N_{\text{spin-up}} - N_{\text{spin-down}}$) from the energy of -2.55 to 0 eV is integrated, which is dominated by the non-bonding state (O p_π). It is found that the unpaired O p_π state is increased by $\sim 0.21 e^-$ with the negative charge. This indicates that the ligand oxygens have more unpaired electrons and the radical character of oxygen is increased with the negative charge. That is consistent with the creation of $\text{O}(-)$ species with more unpaired O p non-bonding electrons under high pH.



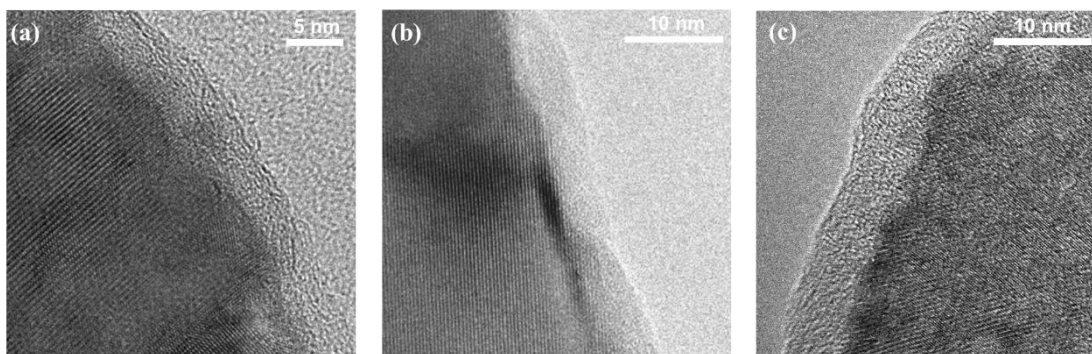
Supplementary Fig. 1. The 1st and 2nd CVs of pristine $\text{Co}_{3-x}\text{Fe}_x\text{O}_4$ spinel oxides in O_2 -saturated 1 M KOH with a scan rate of 10 mV s^{-1} : (a) Co_3O_4 ; (b) $\text{Co}_{2.75}\text{Fe}_{0.25}\text{O}_4$; (c) FeCo_2O_4 and (d) CoFe_2O_4 .



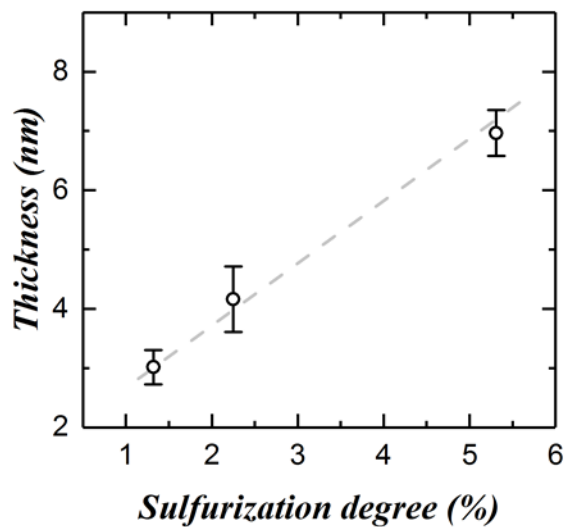
Supplementary Fig. 2. **a, b**, The HRTEM images of Pristine CoFe_2O_4 (a) before and (b) after 500 OER CVs in 1M KOH. **c**, The 500 CV cycles of CoFe_2O_4 of 10 mV s^{-1} in 1 M KOH. The OER CV shows negligible change during 500 cycles.



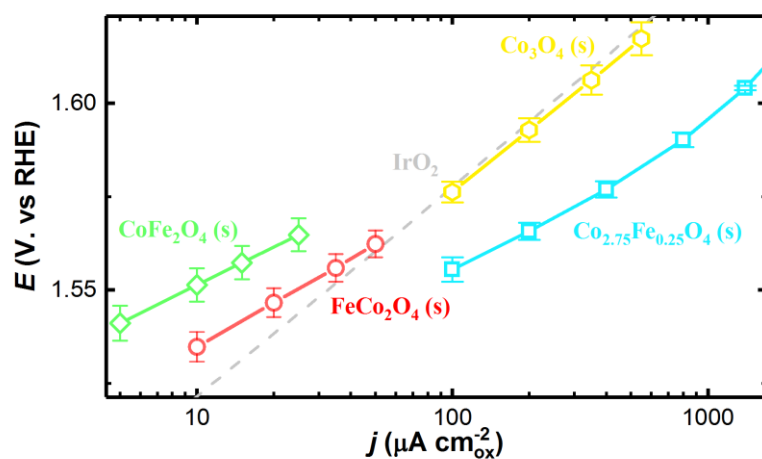
Supplementary Fig. 3. (a, c, e) The pseudo-capacitive region of the CV and (b, d, f) the 2nd cycle of OER CV of $\text{Co}_{2.75}\text{Fe}_{0.25}\text{O}_4$ (S) in different sulfurization degree: (a-b) 5:0.5, (c-d) 5:1 and (e-f) 5:3. The ratio denotes the mass ratio of oxide to sulfur powder in the mixture before the sulfurization.



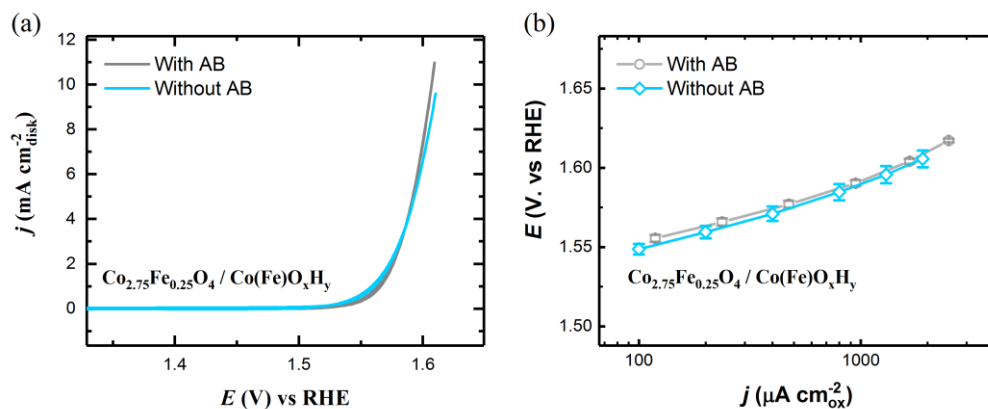
Supplementary Fig. 4. The HRTEM images of the $\text{Co}_{2.75}\text{Fe}_{0.25}\text{O}_4/\text{Co}(\text{Fe})\text{O}_x\text{H}_y$ reconstructed from $\text{Co}_{2.75}\text{Fe}_{0.25}\text{O}_4$ (S) with different sulfurization degree: (a) 5:0.5, (b) 5:1, and (c) 5:3. The ratio denotes the mass ratio of oxide to sulfur powder in the mixture before the sulfurization. No Nafion binder or carbon was added.



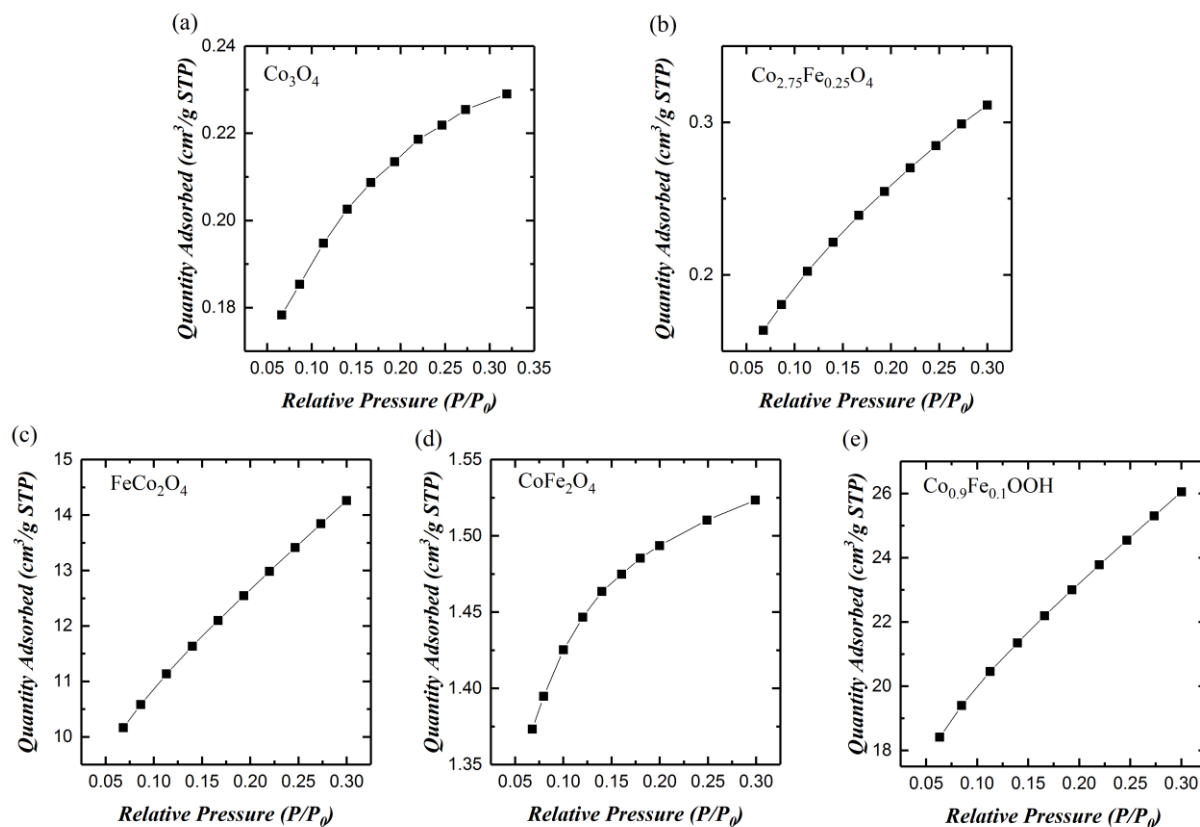
Supplementary Fig. 5. The plot of the thickness of oxyhydroxide layer after reconstruction versus the sulfidization degree of $\text{Co}_{2.75}\text{Fe}_{0.25}\text{O}_4$ oxide. The sulfidization degree of $\text{Co}_{2.75}\text{Fe}_{0.25}\text{O}_4$ oxide is determined by the ICP-OES measurement.



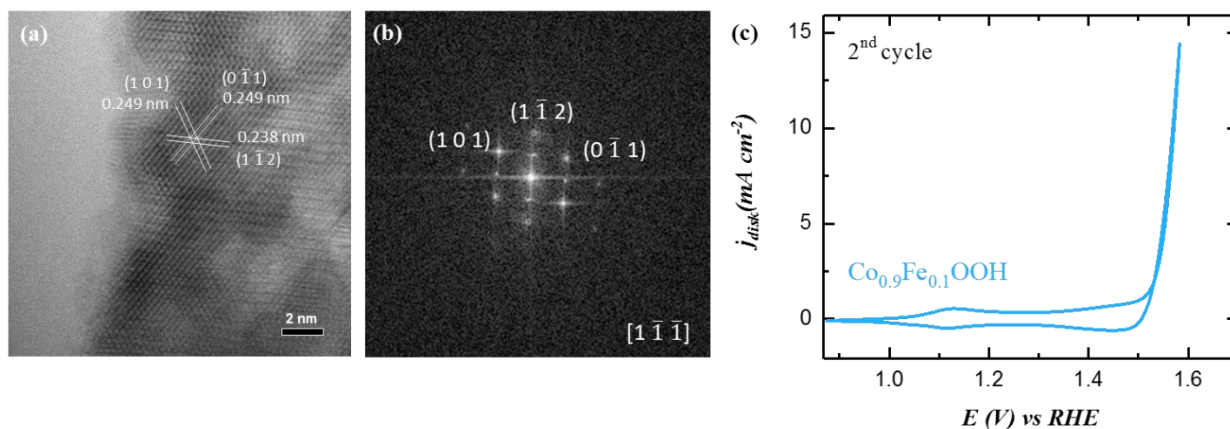
Supplementary Fig. 6. The Tafel plots in specific activity of $\text{Co}_{3-x}\text{Fe}_x\text{O}_4$ (s) ($x=0\sim2.0$), and IrO_2^{22} . The plots are given after oxide surface area normalization, capacitance correction, and iR correction. The error bars represent the standard deviation from three independent measurements.



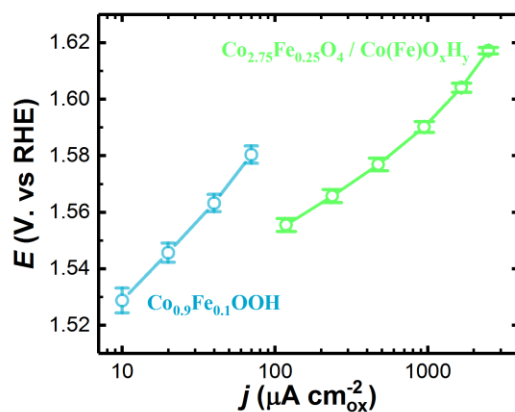
Supplementary Fig. 7. (a) The 2nd LSV of $\text{Co}_{2.75}\text{Fe}_{0.25}\text{O}_4/\text{Co}(\text{Fe})\text{O}_x\text{H}_y$ with and without mixing with carbon in O_2 -saturated 1 M KOH. (b) The Tafel plots of the OER specific activity of $\text{Co}_{2.75}\text{Fe}_{0.25}\text{O}_4/\text{Co}(\text{Fe})\text{O}_x\text{H}_y$ with and without mixing with carbon. The error bar represents the standard deviation of three independent measurements.



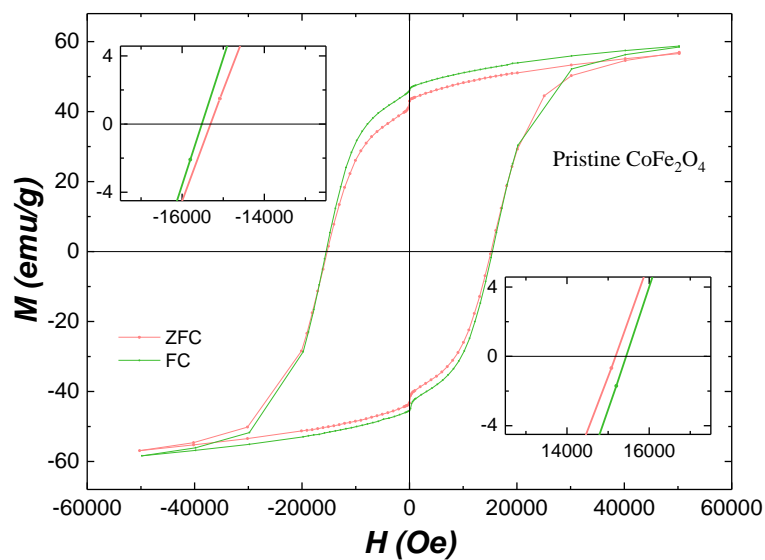
Supplementary Fig. 8. The BET surface area measurements of $\text{Co}_{3-x}\text{Fe}_x\text{O}_4$ spinel oxides. The details about surface area and materials synthesis parameters are summarized in Supplementary Table 1.



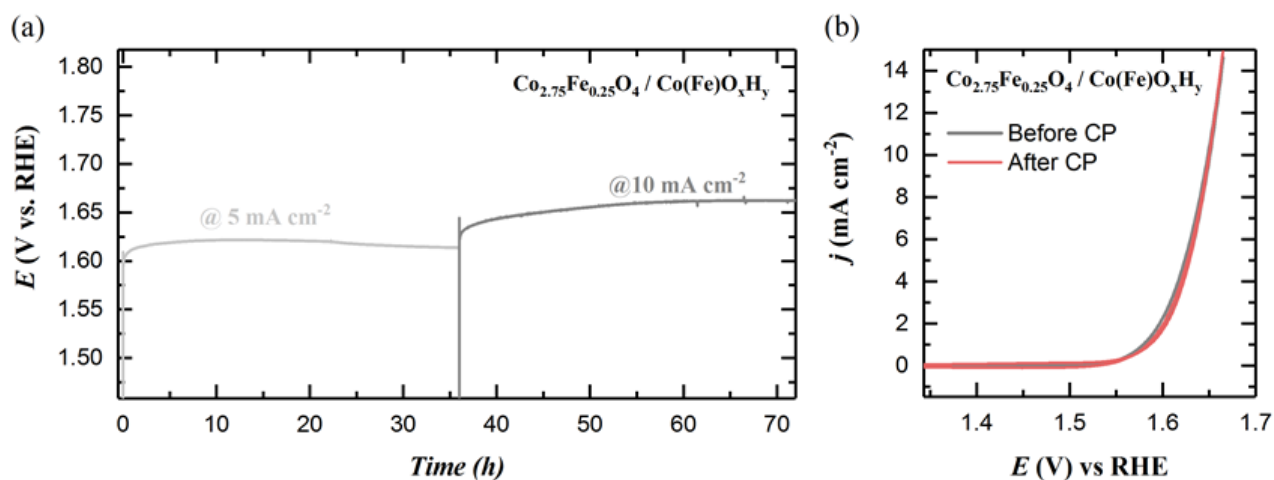
Supplementary Fig. 9. (a) The HRTEM image and (b) the fast Fourier transformed (FFT) pattern of as-prepared $\text{Co}_{0.9}\text{Fe}_{0.1}\text{OOH}$. (c) The cyclic voltammetry (CV) of $\text{Co}_{0.9}\text{Fe}_{0.1}\text{OOH}$ at the steady state with a scan rate of 10 mV s^{-1} in O_2 -saturated 1 M KOH .



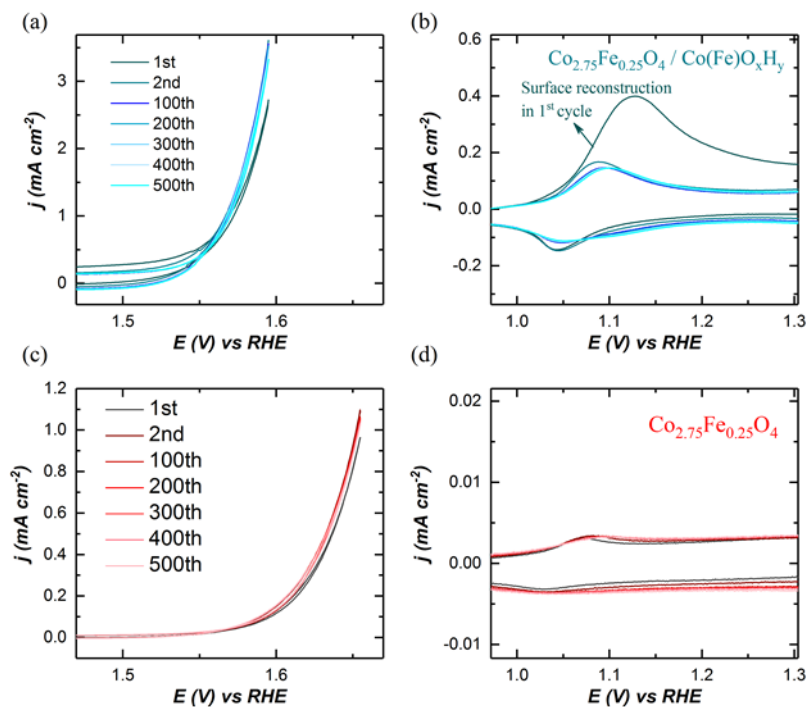
Supplementary Fig. 10. The Tafel plots of the OER specific activity of reconstructed $\text{Co}_{2.75}\text{Fe}_{0.25}\text{O}_4(\text{s})$ (i.e. $\text{Co}_{2.75}\text{Fe}_{0.25}\text{O}_4 / \text{Co}(\text{Fe})\text{O}_x\text{H}_y$) and $\text{Co}_{0.9}\text{Fe}_{0.1}\text{OOH}$. The current density is normalized to the surface area of catalysts determined by BET measurement



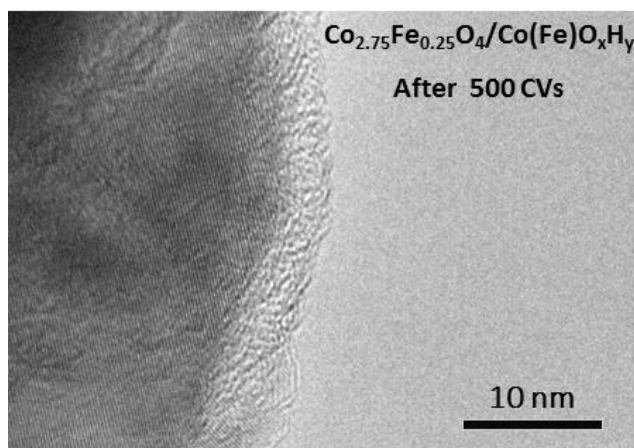
Supplementary Fig. 11. The magnetic hysteresis loop of pristine CoFe_2O_4 under both field-cooled (FC) mode and zero-field-cooled (ZFC) mode.



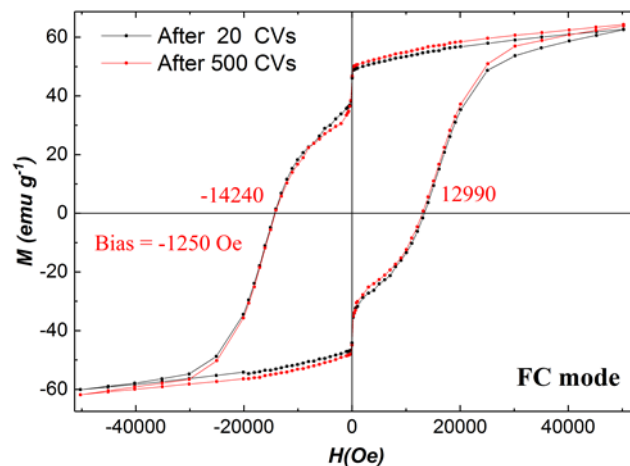
Supplementary Fig. 12. (a) The chronopotentiometry test of $\text{Co}_{2.75}\text{Fe}_{0.25}\text{O}_4/\text{Co}(\text{Fe})\text{O}_x\text{H}_y$ for totally 72 hours under the OER current densities of 5.0 and 10.0 $\text{mA cm}_{\text{disk}}^{-2}$ in 1 M KOH. (b) The CVs (scan rate of 10 mV s^{-1}) of $\text{Co}_{2.75}\text{Fe}_{0.25}\text{O}_4/\text{Co}(\text{Fe})\text{O}_x\text{H}_y$ before and after CP measurement. The electrodes were fabricated without adding carbon.



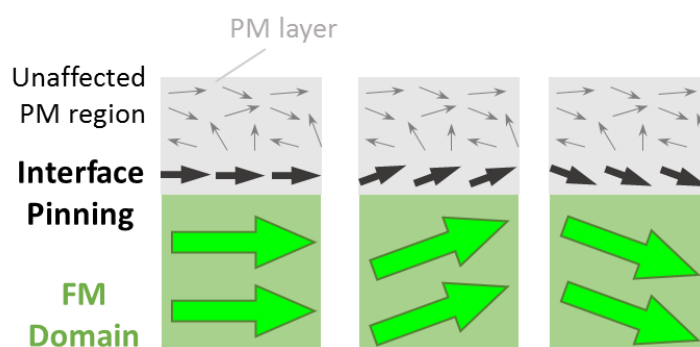
Supplementary Fig. 13. The 500 CVs of (a-b) $\text{Co}_{2.75}\text{Fe}_{0.25}\text{O}_4/\text{Co}(\text{Fe})\text{O}_x\text{H}_y$ and (b-c) $\text{Co}_{2.75}\text{Fe}_{0.25}\text{O}_4$ at scan rate of 10 mV s^{-1} in 1 M KOH. In Figure (a) and (b), the 1st cycle involves the reconstruction from the pre-catalyst (sulfurized $\text{Co}_{2.75}\text{Fe}_{0.25}\text{O}_4$) to the desired catalyst ($\text{Co}_{2.75}\text{Fe}_{0.25}\text{O}_4/\text{Co}(\text{Fe})\text{O}_x\text{H}_y$) and thus its CV profile is different from other subsequent cycles.



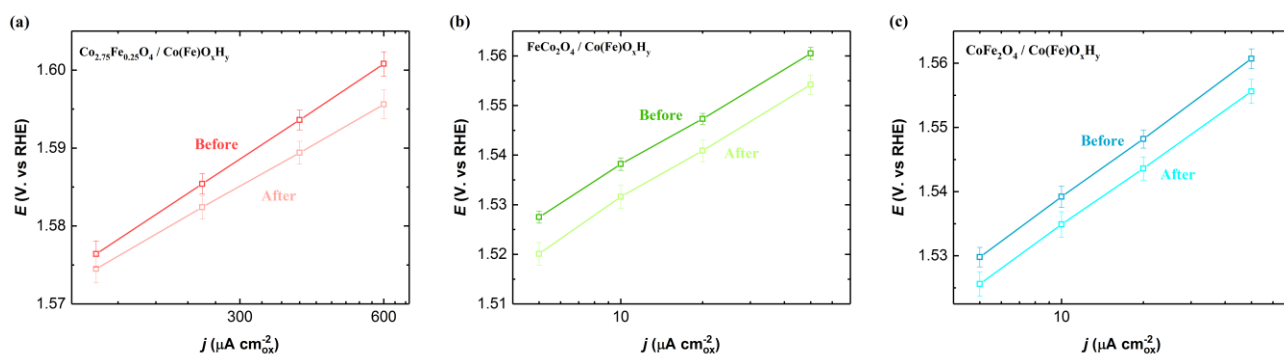
Supplementary Fig. 14. The HRTEM of $\text{Co}_{2.75}\text{Fe}_{0.25}\text{O}_4/\text{Co}(\text{Fe})\text{O}_x\text{H}_y$ after 500 CV cycles.



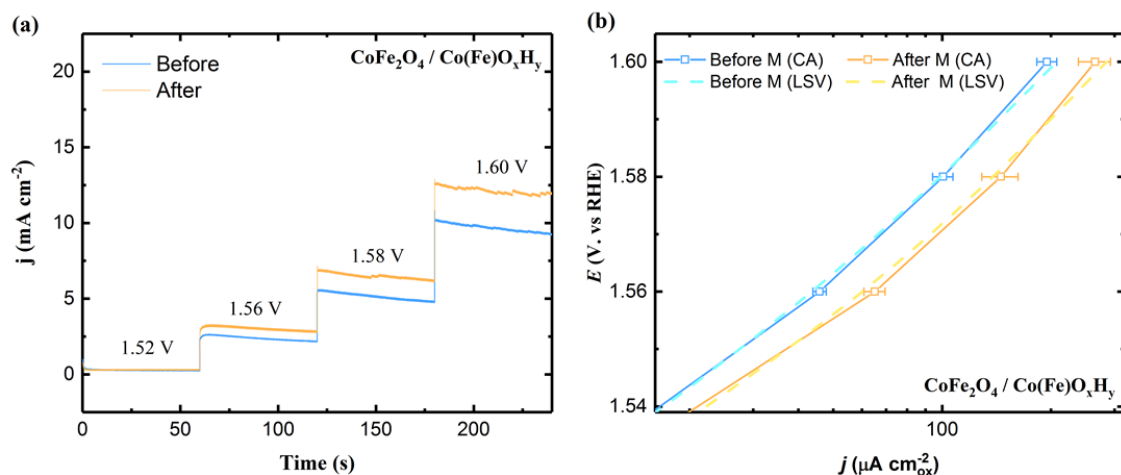
Supplementary Fig. 15. The hysteresis loop of CoFe₂O₄/Co(Fe)O_xH_y under field-cooled (FC) mode after 20 and 500 CV cycles.



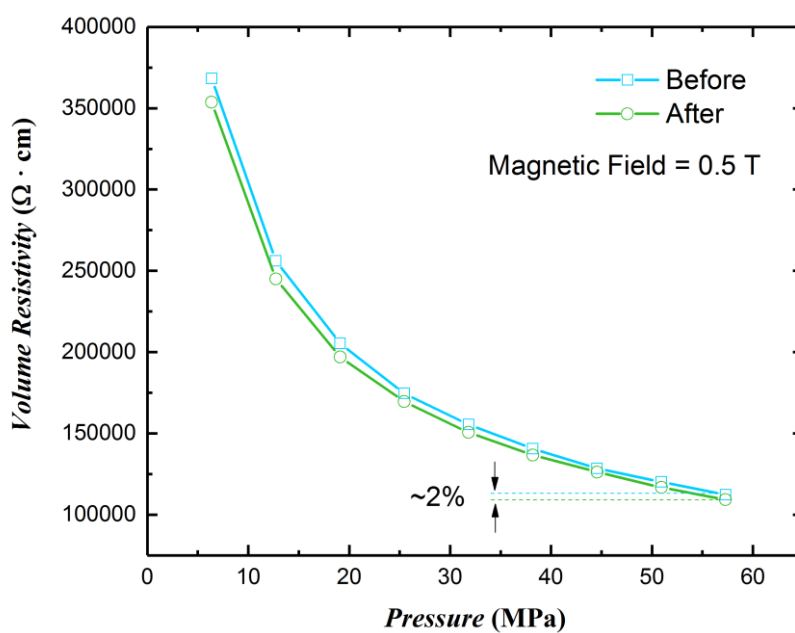
Supplementary Fig. 16. The schematic illustration of the spin pinning effect at the interface between ferromagnetic (FM) magnetic domains and the paramagnetic (PM) layer. The spins in a paramagnetic material are naturally disordered. The spins in the FM magnetic domains of a ferromagnetic materials are naturally highly aligned.



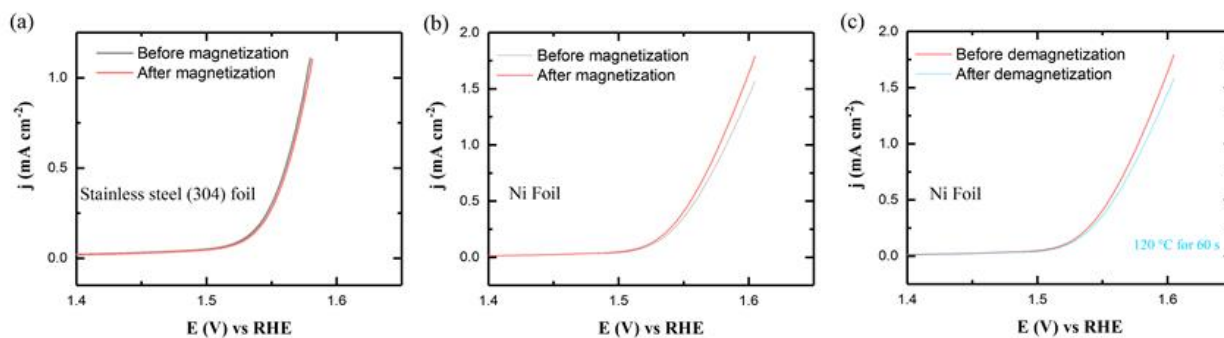
Supplementary Fig. 17 The Tafel plots of (a) Co_{2.75}Fe_{0.25}O₄/Co(Fe)O_xH_y, (b) FeCo₂O₄/Co(Fe)O_xH_y and (c) CoFe₂O₄/Co(Fe)O_xH_y before and after magnetization under 0.5 T for 15 min. The error bars represent the standard deviation from three independent measurements.



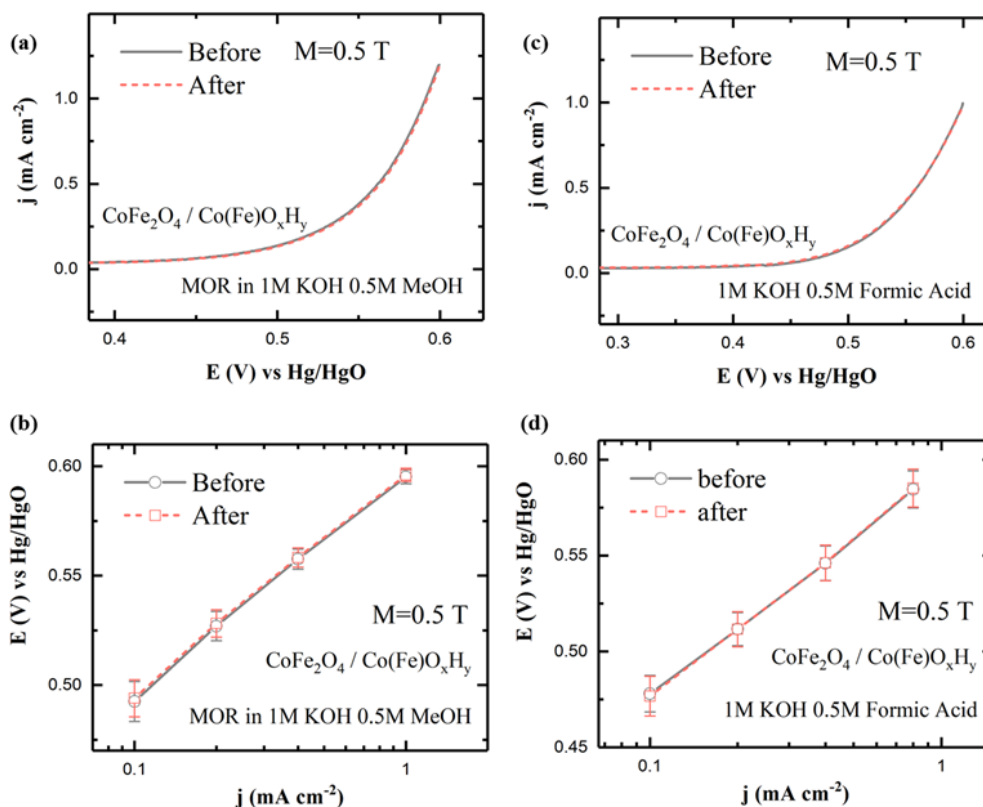
Supplementary Fig. 18. (a) The chronoamperometry of the reconstructed CoFe_2O_4 (i.e. $\text{CoFe}_2\text{O}_4/\text{Co(Fe)O}_x\text{H}_y$) before and after magnetization (0.5T, 15 min). (b) The OER Tafel plots of $\text{CoFe}_2\text{O}_4/\text{Co(Fe)O}_x\text{H}_y$ determined by CA and LSV (scan rate of 10 mV s^{-1}) measurements.



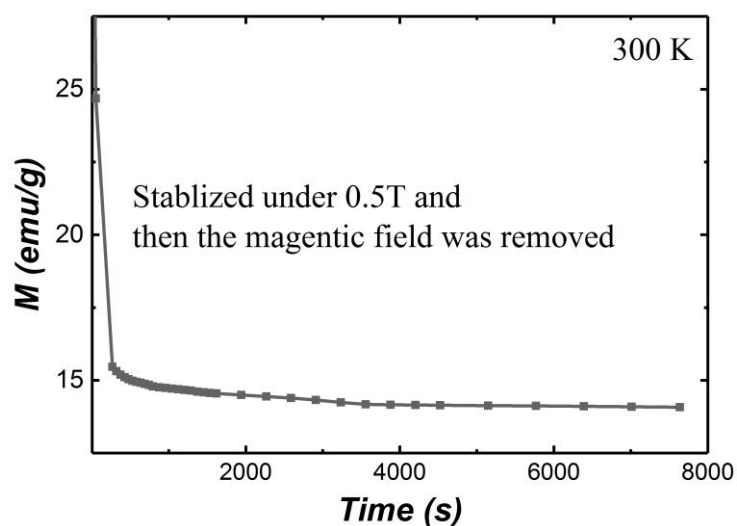
Supplementary Fig. 19. The magnetoresistance measurement of CoFe_2O_4 before and after applying magnetic field of 0.5 T for 15 min.



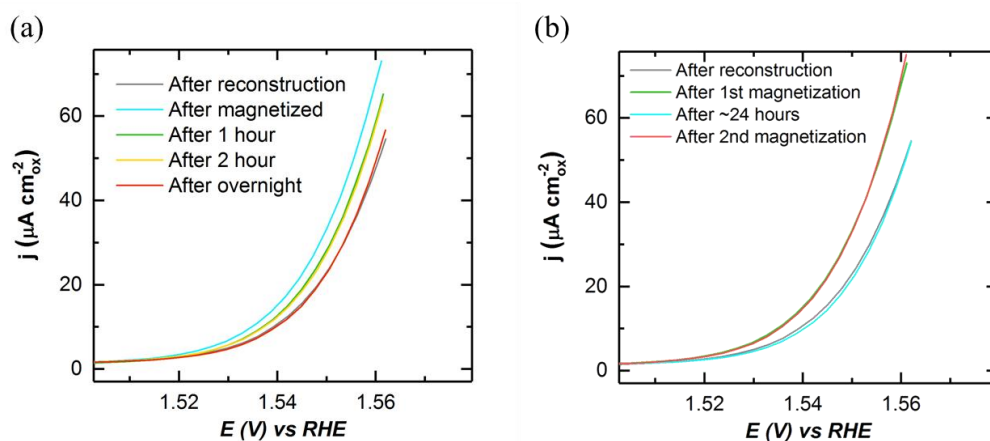
Supplementary Fig. 20. (a) The steady state (50th) LSV of stainless-steel (304) foil in 1 M KOH before magnetization and the LSV after magnetization (under 0.5 T for 15 min). (b) The steady state (50th) LSV of Ni foil in 1 M KOH and the LSV after magnetization (under 0.5 T for 15 min). (c) The LSV of magnetized Ni foil before and after demagnetization.



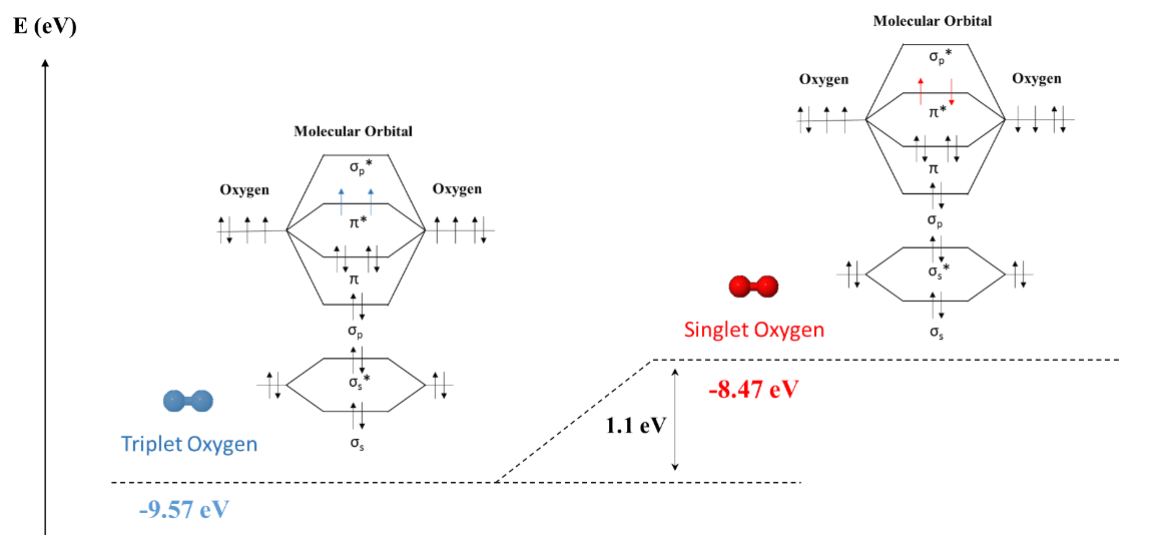
Supplementary Fig. 21. The electrochemical performance of CoFe₂O₄/Co(Fe)O_xH_y and the corresponding Tafel plots before and after magnetization under 0.5 T for 15 min for (a-b) methanol oxidation reaction (MOR) and (c-d) Formic acid oxidation (FOR). The error bars represent the standard deviation of at least three independent measurements.



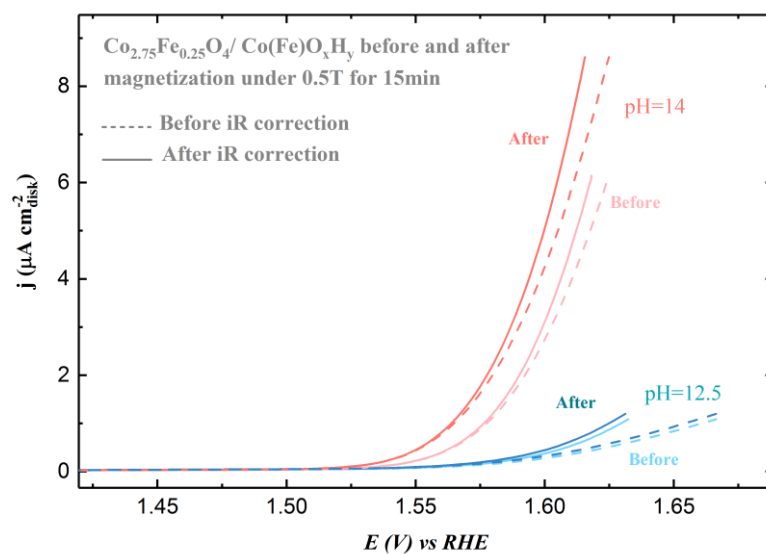
Supplementary Fig. 22. The magnetization of $\text{CoFe}_2\text{O}_4/\text{Co}(\text{Fe})\text{O}_x\text{H}_y$ after removing a constant magnetic field of 0.5T.



Supplementary Fig. 23. (a) The OER LSV of CoFe_2O_4 (s) after reconstruction, magnetization under 0.5T for 15 min, holding for 1 hour, holding for 2 hours and holding for overnight. (b) The re-activation of $\text{CoFe}_2\text{O}_4/\text{Co}(\text{Fe})\text{O}_x\text{H}_y$ by magnetizing it again.

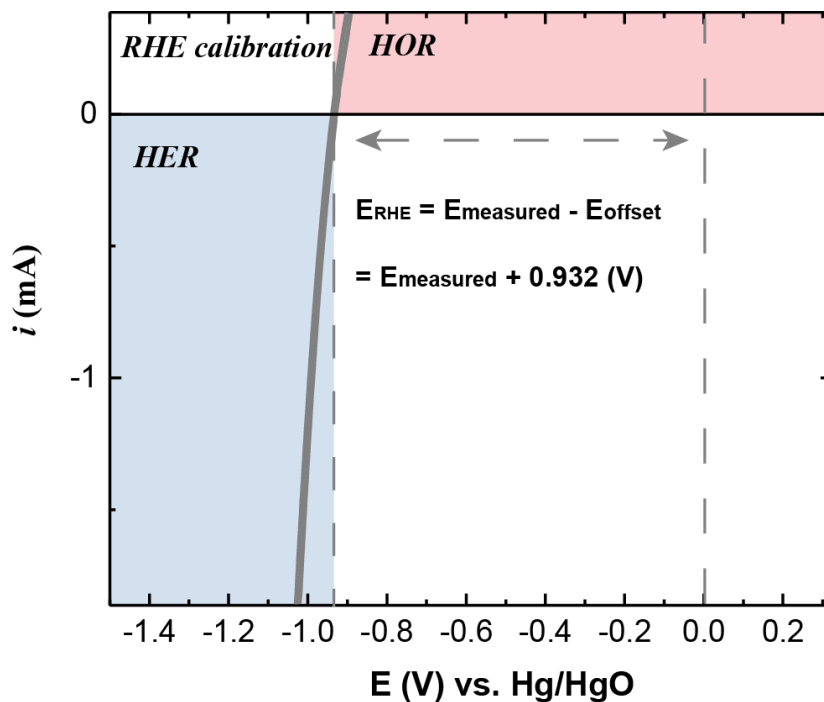


Supplementary Fig. 24. The energy diagram of generating triplet oxygen versus generating singlet oxygen.

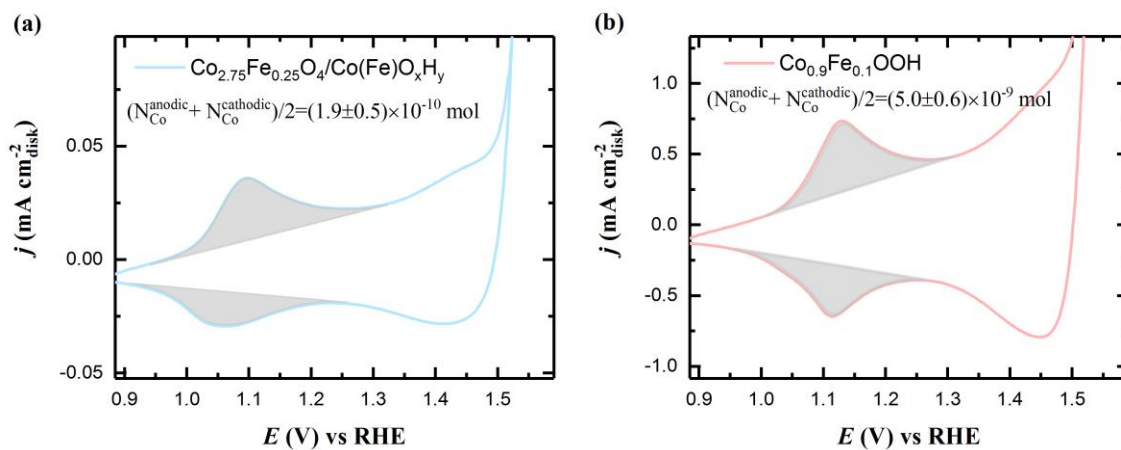


Supplementary Fig. 25. The iR correction of the OER LSV of $\text{Co}_{2.75}\text{Fe}_{0.25}\text{O}_4 / \text{Co(Fe)O}_x\text{H}_y$ in KOH electrolyte with different pH.

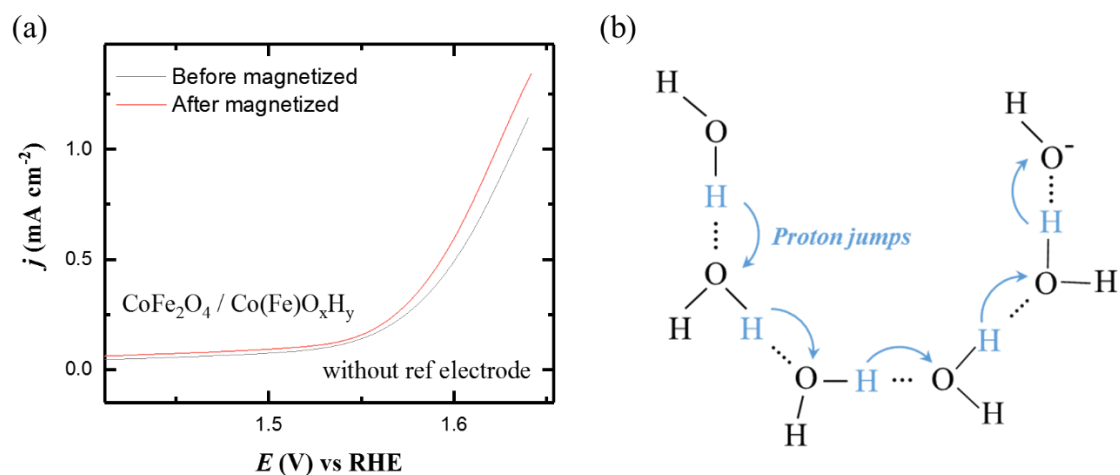
state ($N_{\text{spin-up}} - N_{\text{spin-down}}$) from the energy of -2.55 to 0 eV.



Supplementary Fig. 28. The RHE calibration of the Hg/HgO reference electrode in H₂-saturated 1 M KOH (pH=14.0).



Supplementary Fig. 29. The Co²⁺/Co³⁺ anodic and cathodic peaks in the CVs of (a) Co_{2.75}Fe_{0.25}O₄/Co(Fe)O_xH_y and (b) Co_{0.9}Fe_{0.1}OOH. The N_{Co} is estimated by assuming a one-electron process.⁴



Supplementary Fig. 30. (a) The two-electrode measurement of $\text{CoFe}_2\text{O}_4/\text{Co(Fe)O}_x\text{H}_y$ before and after magnetization under 0.5 T for 15 min. The reference electrode is not used in the two-electrode system. (b) The mechanism of proton hopping (jump) for OH^- in aqueous solution.²⁵

Supplementary Table 1. ICP result of $\text{Co}_{3-x}\text{Fe}_x\text{O}_4$ (s)

	Elemental ratio			Sulfurization degree
	Co%	Fe%	S%	
Co_3O_4 (s) (5:1)	97.09%	0	2.91%	2.06%
$\text{Co}_{2.75}\text{Fe}_{0.25}\text{O}_4$ (s) (5:0.5)	90.16%	8.11%	1.73%	1.32%
$\text{Co}_{2.75}\text{Fe}_{0.25}\text{O}_4$ (s) (5:1)	89.29%	8.04%	2.67%	2.25%
$\text{Co}_{2.75}\text{Fe}_{0.25}\text{O}_4$ (s) (5:3)	85.68%	7.71%	6.61%	5.31%
FeCo_2O_4 (s) (5:1)	64.52%	32.26%	3.23%	2.25%
CoFe_2O_4 (s) (5:1)	32.47%	63.96%	3.57%	2.75%

The ratio denotes the mass ratio of oxide to sulfur during the sulfurization

Supplementary Table 2. Summary synthesis parameters and surface areas (A_s) of $\text{Co}_{3-x}\text{Fe}_x\text{O}_4$ spinel oxides.

	Calcination temperature (°C)	Calcination time	Mass for BET Measurement (g)	A_s ($\text{m}^2 \text{g}^{-1}$)	STD
Co_3O_4	600	6 hours	1.1799	0.81	0.02
$\text{Co}_{2.75}\text{Fe}_{0.25}\text{O}_4$	600	6 hours	0.705	1.10	0.08
FeCo_2O_4	400	6 hours	0.1717	43.16	1.23

CoFe ₂ O ₄	500	6 hours	0.1436	19.17	0.51
Co _{0.9} Fe _{0.1} OOH	90	24 hours	0.3447	80.85	2.11

Supplementary Table 3. The correction of zero point energy and entropy of the adsorbed and gaseous species.

	ZPE(eV)	TS(eV)
*OOH	0.35	0
*O	0.05	0
*OH	0.31	0.01
H ₂ O	0.56	0.67
H ₂	0.27	0.41

Supplementary Table 4. The magnetizations of Co and O in *OH, *O, *OOH and *OO with and without negative charge.

		*OH	*O	*OOH	*OO
O	Without charge	0.343	0.828	0.373; 0.190	-0.725; -0.818
	With negative charge	0.320	0.767	0.322; 0.143	-0.693; -0.765
Co	Without charge	2.958	1.126	0.332	2.579
	With negative charge	2.934	1.369	0.500	2.501

The O1 and O2 denote the oxygen in the *OH, *O, *OOH and *OO intermediates.

Reference

1. Wu, T., et al., Iron-facilitated dynamic active-site generation on spinel CoAl₂O₄ with self-termination of surface reconstruction for water oxidation. *Nature Catalysis* **2**, 763-772 (2019).
2. Wei, C., et al., Recommended Practices and Benchmark Activity for Hydrogen and Oxygen Electrocatalysis in Water Splitting and Fuel Cells. *Advanced Materials* **31**, 1806296 (2019).
3. Burke, M. S., et al., Cobalt–Iron (Oxy)hydroxide Oxygen Evolution Electrocatalysts: The Role of Structure and Composition on Activity, Stability, and Mechanism. *J. Am. Chem. Soc.* **137**, 3638-3648 (2015).
4. Surendranath, Y.; Kanan, M. W.; Nocera, D. G., Mechanistic Studies of the Oxygen Evolution Reaction by a Cobalt-Phosphate Catalyst at Neutral pH. *Journal of the American Chemical Society* **132**, 16501-16509 (2010).

5. Roy, C., et al., Impact of nanoparticle size and lattice oxygen on water oxidation on NiFeOxHy. *Nature Catalysis* **1**, 820-829 (2018).
6. Trotochaud, L.; Young, S. L.; Ranney, J. K.; Boettcher, S. W., Nickel–iron oxyhydroxide oxygen-evolution electrocatalysts: the role of intentional and incidental iron incorporation. *Journal of the American Chemical Society* **136**, 6744-6753 (2014).
7. Chen, Y., et al., Exceptionally active iridium evolved from a pseudo-cubic perovskite for oxygen evolution in acid. *Nature Communications* **10**, 572 (2019).
8. Kresse, G.; Furthmüller, J., Efficient iterative schemes for ab initio total-energy calculations using a plane-wave basis set. *Physical Review B* **54**, 11169-11186 (1996).
9. Kresse, G.; Hafner, J., Ab initio. *Physical Review B* **49**, 14251-14269 (1994).
10. Blöchl, P. E., Projector augmented-wave method. *Physical Review B* **50**, 17953-17979 (1994).
11. Perdew, J. P.; Burke, K.; Ernzerhof, M., Generalized Gradient Approximation Made Simple. *Phys. Rev. Lett.* **77**, 3865-3868 (1996).
12. Zhang, Y.; Yang, W., Comment on "Generalized Gradient Approximation Made Simple". *Physical Review Letters* **80**, 890-890 (1998).
13. Hammer, B.; Hansen, L. B.; Nørskov, J. K., Improved adsorption energetics within density-functional theory using revised Perdew-Burke-Ernzerhof functionals. *Physical Review B* **59**, 7413-7421 (1999).
14. Monkhorst, H. J.; Pack, J. D., Special points for Brillouin-zone integrations. *Physical review B* **13**, 5188 (1976).
15. Nørskov, J. K., et al., Origin of the overpotential for oxygen reduction at a fuel-cell cathode. *The Journal of Physical Chemistry B* **108**, 17886-17892 (2004).
16. Li, Y., et al., One-Step Synthesis of a Coral-Like Cobalt Iron Oxyhydroxide Porous Nanoarray: An Efficient Catalyst for Oxygen Evolution Reactions. *ChemPlusChem* **84**, 1681-1687 (2019).
17. Lee, D. H., et al., Asymmetric Transport Mechanisms of Hydronium and Hydroxide Ions in Amorphous Solid Water: Hydroxide Goes Brownian while Hydronium Hops. *The Journal of Physical Chemistry Letters* **5**, 2568-2572 (2014).
18. Lin, M.-Y.; Hourng, L.-W.; Kuo, C.-W., The effect of magnetic force on hydrogen production efficiency in water electrolysis. *International Journal of Hydrogen Energy* **37**, 1311-1320 (2012).
19. Matsushima, H.; Iida, T.; Fukunaka, Y., Gas bubble evolution on transparent electrode during water electrolysis in a magnetic field. *Electrochimica Acta* **100**, 261-264 (2013).
20. Shimoyama, Y.; Kojima, T., Metal–Oxyl Species and Their Possible Roles in Chemical Oxidations. *Inorganic Chemistry* **58**, 9517-9542 (2019).
21. Diaz-Morales, O.; Ferrus-Suspedra, D.; Koper, M. T. M., The importance of nickel oxyhydroxide deprotonation on its activity towards electrochemical water oxidation. *Chemical Science* **7**, 2639-2645 (2016).
22. Lee, Y., et al., Synthesis and Activities of Rutile IrO₂ and RuO₂ Nanoparticles for Oxygen Evolution in Acid and Alkaline Solutions. *J. Phys. Chem. Lett.* **3**, 399-404 (2012).